UNIVERISTY OF OKLAHOMA GRADUATE COLLEGE

Monazite Fission-Track Dating of Erosion and Tectonics in the Nepalese Himalaya

A THESIS

SUBMITTED TO THE GRADUATE FACULTY

In partial fulfillment of the requirements for the degree of

MASTER OF SCIENCE

By SOFIA BARTH

Norman, Oklahoma

2025

Monazite Fission-Track Dating of Erosion and Tectonics in the Nepalese Himalaya

A THESIS APPROVED FOR THE

SCHOOL OF GEOSCIENCES

BY THE COMMITTEE CONSISTING OF

Dr. GILBY JEPSON, Chair

Dr. SARAH GEORGE

Dr. NETRA REGMI

Acknowledgements

I extend my gratitude to my advisor, Dr. Gilby Jepson, for his dedication, support and constant wisdom throughout the process of this research. His commitment to this field of geology is uniquely motivating, and I will take his lessons of efficiency, work ethic, passion, and patience with me in all future careers. His curiosity to this research project will pave the way for a new method of thermochronology, speaking to his devotion and enthusiasm for the overall progress of geosciences. Dr. Gilby Jepson is an inspiring scientist, and I will always be honored to have been one of his students. I want to thank Dr. Sarah George and Dr. Netra Regmi for their commitment, insight and guidance throughout this research. Their support and lessons in the field reminded me of my fascination and love for geology and were they inspiring and motivating mentors throughout this process. I lastly want to thank the STOUT and CLAST lab groups for the never-ending support and friendship. The encouragement of this lab group was unique, and I am eternally proud of the scientists we have grown to be.

Table of Contents

Figures

Abstract

A modern orogenic system represents the culmination of tectonic and surface processes over geological time, posing challenges in isolating direct mechanisms and associated timing of relief formation. Modern relief-forming processes are typically dominated by more recent, low-magnitude erosion/exhumation events (<1 – 2 km), which are difficult to resolve with established low-temperature thermochronology and cosmochemistry methods. Monazite fission-track (MzFT) is a relatively new low-temperature thermochronometer with a laboratory assessed partial annealing zone of 140 – -70 °C. Field based estimates, however, have found MzFT to be a useful proxy for cooling through <50 – 25 °C and related to exhumation in the upper 1 – 2 km of the crust. Given the uncertainties between laboratory- and field-based estimates, interpreting a MzFT age can be challenging due to the relative contributions of fault-driven denudation, surface processes and surface temperatures. To assess the applicability of MzFT to resolving upper crustal exhumation, we apply MzFT to the Nepalese Himalaya, an actively uplifting and highly erosive orogenic system associated with a cool subtropical to temperate climate. We focus on the well-studied Kali Gandaki River in central Nepal, which has been previously targeted by a range of established low-temperature thermochronometers. We collected four MzFT samples, with three samples being part of an elevation profile (2498 – 2966 m) and two apatite fission-track (AFT) samples from within the Greater Himalayan Sequence across the Ramgarh Thrust, Main Central Thrust and South Tibetan Detachment. We integrate MzFT data with existing low-temperature thermochronology data and single-grain monazite and apatite geochemistry to isolate incision and/or faulting processes as the driver of rock cooling. MzFT data yield ages of ~0.4 – 0.09 Ma, which we interpret to correlate with recent movement of the Main Frontal Thrust since at least ~280 k.y., and concurrent river incision of the Kali Gandaki drainage.

Introduction

The modern topography is a function of tectonic and surface processes interacting across geologic time. Tectonic processes create rock uplift, which couples with the hydroclimate to drive erosion and modulate exhumation (e.g., Molnar & England, 1990; Sobel et al., 2003). As a result, the relative influence of tectonic and surface processes on the modern topography are inherently coupled with changes in one (e.g., increased uplift) balanced by a corresponding change in the other (e.g., increased erosion). It is the interplay among climate, tectonics and erosion that complicates the relationship between geologic processes and the (paleo)topography. This issue is heightened in regions like the Himalaya, which hosts some of the highest shortening rates (e.g., ~20-25 mm/yr in Eastern Himalaya (Long et al., 2012) and intense, seasonal precipitation (up to 4300 mm/yr; e.g., Burbank et al., 2003).

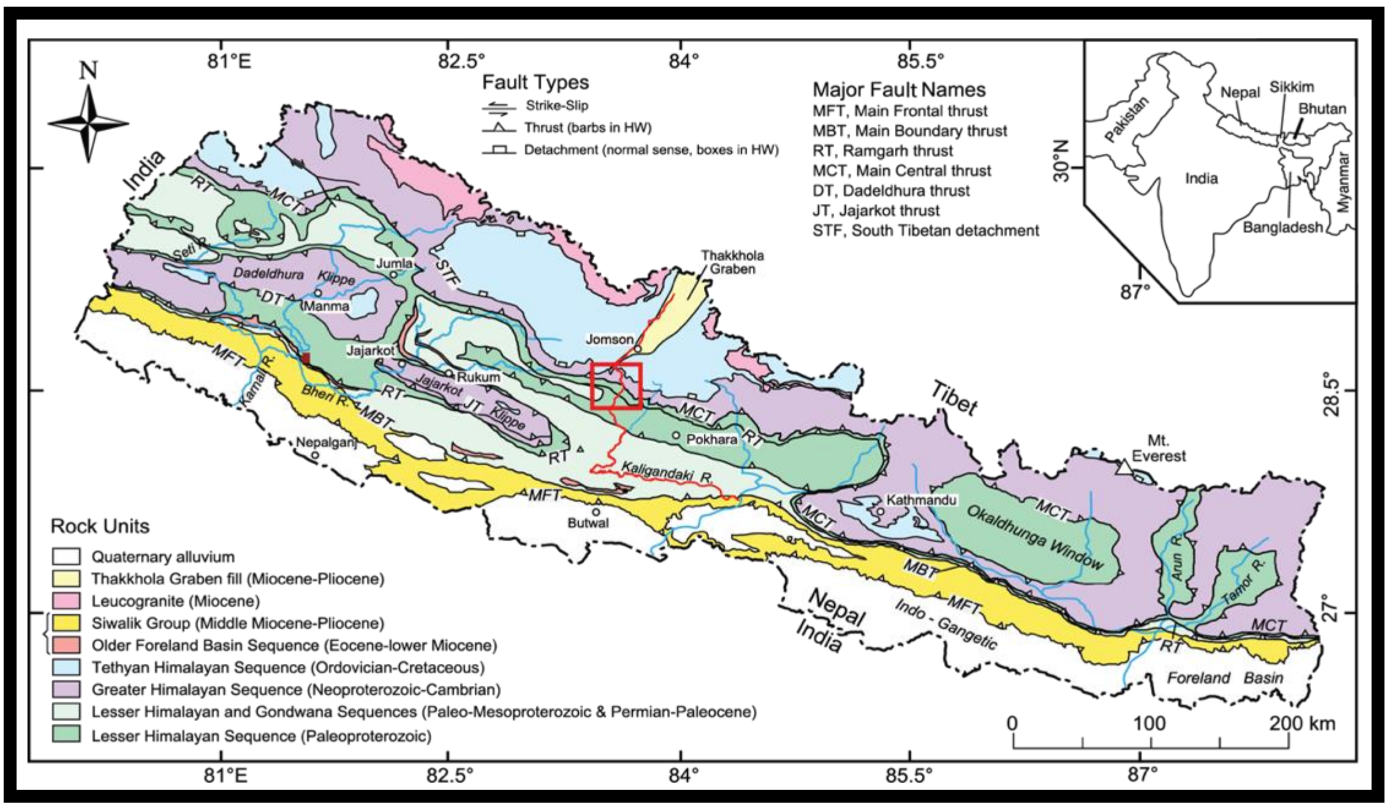

Figure 1. Geologic Map of Nepal, modified from DeCelles et al., (2020) and Sherpa et al., (2023). Red line shows the Kali Gandaki River and the red rectangle outlines the study area.

The Nepalese Himalaya provides a unique study area to examine the interplay between climatic surface processes and shallow crustal tectonic mechanisms, as it is tectonically active, young, and a highly erosive. This region hosts some of the world's most prominent and active river drainages, creating a distinct pattern of incision during the rapid uplift of the Greater Himalayas (Lavé and Avouac, 2001). Connections between incision and uplift have been an ongoing focus of research including how erosional asymmetry correlates with near-surface variations in rock uplift (Beaumont et al., 2001; Whipple, 2009). To investigate this question, we work in the northern Kali Gandaki River in Central Nepal, because there is a tightly coupled relationship between river incision and exhumation along major thrust systems, including the Main Frontal Thrust (MFT), the Main Boundary Thrust (MBT), the Ramgarh Thrust (RT), the Main Central Thrust (MCT), the Dadeldhura Thrust (DT), and the South Tibetan Detachment (STD) (Pye et al., 2022). The Kali Gandaki River flows along a NNE-SSW axis, sculpting one of the deepest gorges on earth (Pye et al., 2022). The Kali Gandaki River has been central to the discussion of the relative contribution of tectonic and climate processes on exhumation of the Himalaya (DeCelles et al., 2020; Pye et al., 2022, 2023).

Our understanding of how exhumation changes through geologic time has been shaped by low-temperature thermochronology (Braun et al., 2006). Low-temperature thermochronology tracks cooling through the upper-crust (~12-3 km) and is widely used in the Himalaya to understand shortening and erosive processes (Robinson et al., 2006; Thiede and Ehlers, 2013). Despite low temperature sensitivity of modern thermochronometers down to ~40°C (~2 km), most thermochronometers record passage through closure temperatures that are too high to record significant relief forming events (~120 – 40°C; Jepson et al., 2025). To isolate the relative contribution of tectonic and surface processes on the modern relief, we require a system which can resolve cooling through the upper ~1-2 km of Earth's crust. Monazite fission track (MzFT) is a new low temperature thermochronometer with a documented partial annealing zone (temperature sensitivity) of 143 – -71 °C (Weise et al., 2009; Jones et al., 2021). However, applied studies have identified that MzFT likely records cooling through temperatures of < 50-25 °C or 2 – 1 km in the Earth's crust (Jones et al., 2023; Jepson et al., 2025). As a result, MzFT can be used to understand the timing of exhumation and erosion through the uppermost crust (Jepson et al., 2025). Here, we look at the relative roles of faulting and river incision in the Kali Gandaki to bridge the gap between tectonic and relief forming processes.

Geologic Background

The Himalaya formed as a result of the Cenozoic accretion of Indian continent with the Eurasian continent. The timing of collision between the Indian and Eurasian continents, caused by subduction of the Neo-Tethyan Ocean in the late Cretaceous, is often debated, but generally accepted to have occured between ~60 Ma and ~45 Ma (DeCelles et al., 2014; Kapp and DeCelles, 2019). Regardless of the precise timing, the India-Asia collision caused significant shortening accommodated by north Indian Proterozoic to Mesozoic igneous, metamorphic and sedimentary rocks (e.g., Gaetani and Garzanti, 1991; Cawood et al., 2007; Hodges, 2000). In Nepal, these rocks form longitudinal belts of rocks which are separated by major faults and shear zones (e.g., DeCelles et al., 2020).

The northernmost tectonostratigraphic package in Nepal is the Tethyan Himalayan Sequence (Fig 1a; DeCelles et al., 2020). The Tethyan Himalayan Sequence is Ordovician to Cretaceous in age (510 - 470 Ma; DeCelles et al., 2020), consisting of an older, upper-greenschist to lower-amphibolite facies, siliciclastic group and a younger, unmetamorphosed, carbonite-rich group (Garzanti, 1999; DeCelles et al., 2020). The Tethyan Himalaya is bounded to the north by the Indus Tsangpo Suture, the suture between India and Asia (Kellett et al., 2019), and to the south by the South Tibetan Detachment (STD) system. The STD is a zone of low-angle, parallel, continuous, top-to-the-NE, normal-sense faults tracing ~2000 km along the Himalayas (Soucy La Roche et al., 2018; Kellett et al., 2019; DeCelles et al., 2020). This shear zone separates the Tethyan Himalayan Sequence from the Greater Himalayan Sequence.

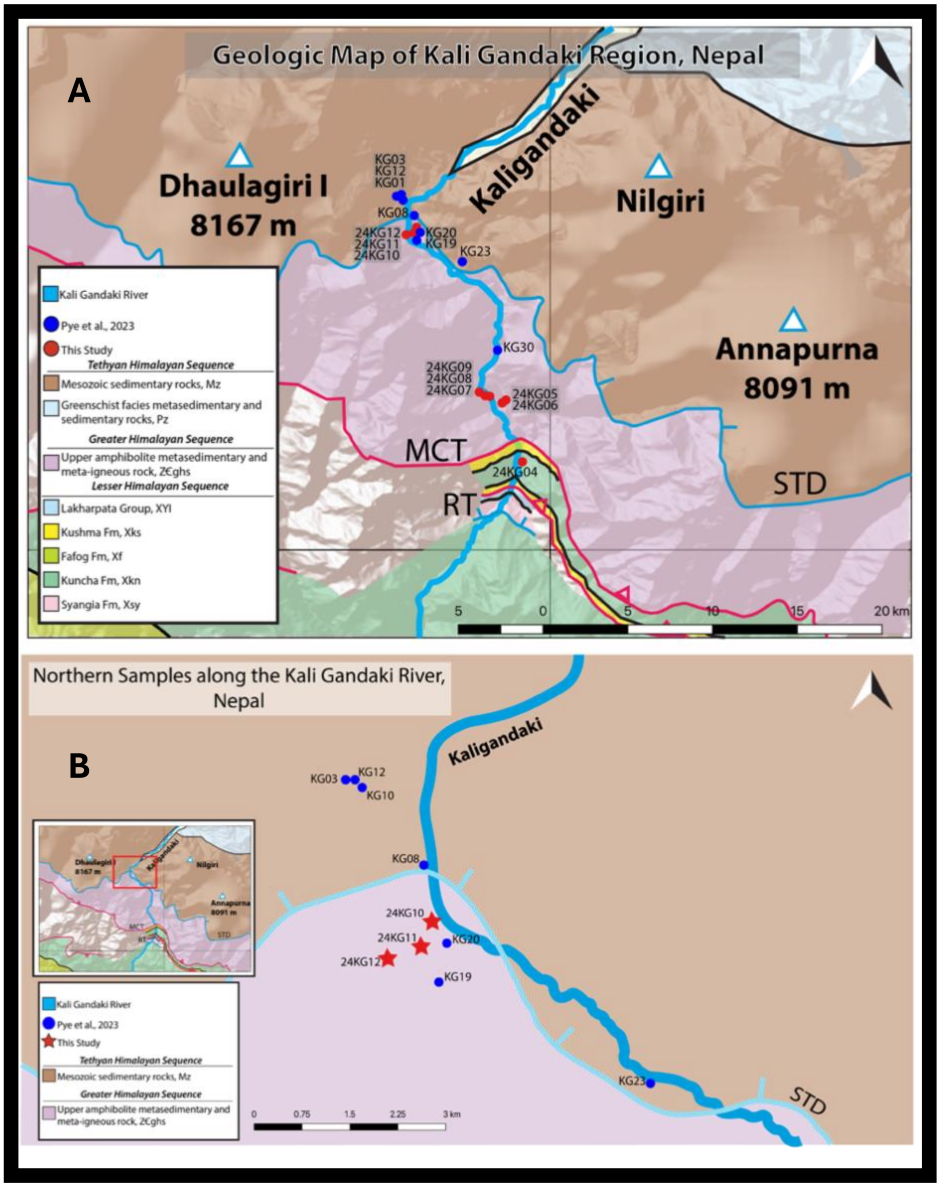

Figure 2. A) Simplified geologic map of the study area, modified from DeCelles et al., 2020 B) Inset map of samples 24KG12, 24KG11 and 24KG10 locations

The Greater Himalayan Sequence (GHS) is Neoproterozoic to Cambrian in age and consists of an upper-amphibolite facies package and an upper-greenschist to lower-amphibolite facies package (DeCelles et al., 2020). Units in this sequence include a schist and gneiss with minor quartzite unit (Unit I), a calc-gneiss (Unit II) and an Ordovician augen gneiss (Unit III) (Soucy La Roche et al., 2018; DeCelles et al., 2020). The GHS is bounded to the north by the STD and the south by the Main Central Thrust (MCT). The MCT is a top-to-the-SW, >1km thick shear zone (Soucy La Roche et al., 2018; DeCelles et al., 2020). The precise extent of the MCT across the Himalaya is controversial (DeCelles et al., 2020). The MCT is the boundary between the Greater Himalayan Sequence and the Lesser Himalayan Sequence.

The Lesser Himalayan Sequence (LHS) has an approximate age of ~1912 – 1300 Ma, and can be divided into two packages: the Lower LHS and Upper LHS (Gehrels et al., 2011; DeCelles et al., 2020). The Lower LHS includes the Kuncha/Ranimata, Kushma and Fafog

Formations, and the Ulleri Gneiss, which are mainly composed of quartzite and phyllite. The Upper LHS includes the Galyang Formation, the Syangia Formation, and the Lakharpata Group, which are mainly composed of a phyllite, quartzite and dolostone (DeCelles et al., 2020). In this region of study, the LHS is bounded to the north by the Main Central Thrust, and the Ramgarh Thrust (RT) to the south (DeCelles et al., 2020). The RT is ~1.5 – 3.1 km thick and has displacement on the order of ~100 km, carrying the Kuncha, Ranimata, Kushma and Fafog Formations (Robinson et al., 2006; DeCelles et al., 2020). Exposures of the RT are variably folded into large synforms and antiforms, including the prominent Dadeldhura and Jajarkot Klippen (Robinson et al., 2006; DeCelles et al., 2020). South of the RT, still within the Lesser Himalayan Zone is the Main Boundary Thrust (MBT). The MBT is the bounding thrust between the LHS and the southern-most Siwalik Group (DeCelles et al., 2020).

The Siwalik Group, ~14 – 2 Ma, consists of an upward-coarsening arrangement of fluvial siltstone, sandstone and conglomerate, that are divided into the lower, middle and upper Siwalik Group (Robinson et al., 2006; DeCelles et al., 2020). South of the Siwalik Group is the prominent topographic front of the Himalayan thrust belt, the Main Frontal Thrust (MFT) (Lavé and Avouac, 2001; DeCelles et al., 2020). The MFT is made of made of multiple laterally overlapping, top-to-the-south faults (Robinson et al., 2006; Soucy La Roche et al., 2018; DeCelles et al., 2020). Robinson et al., (2006) provides evidence for ~485 – 743 km of shortening from the Main Frontal Thrust at the base of the Sub-Himalaya to the South Tibetan Detachment north of the THS. This young, basal thrust system carries much of the Himalayan strata in its hanging wall, accommodating least ~60% of total Himalayan convergence since at least ~200 ka (Bouscary et al., 2024).

Methods

Low Temperature Thermochronology Background

Fission-track thermochronology is a form of radiometric dating which involves analyzing damage tracks in a mineral lattice produced by spontaneous fission of ^{238}U and its rate of decay. The preservation of fission damage is dependent on temperature (Naeser, 1967). Naeser (1967), Naeser & Fleischer (1975), and Price & Walker (1963) published some of the first conclusions about track etching and density, and how these values correlate to time and temperature of certain minerals. Most often applied to apatite and zircon, fission track thermochronology can indicate the thermal history of the examined sample based on the accumulation, habit, and density of fission tracks in the minerals (Tagami, 2005). The density of tracks suggests the time elapsed since spontaneous fission decay of ^{238}U is preserved in the mineral lattice (Tagami, 2005).

Sample Collection

We collected nine samples from three elevation profiles along the Kali Gandaki River in Central Nepal. Samples 24KG07 (1830 m), 24KG08 (2033 m), and 24KG09 (2230 m) were collected from the Greater Himalayan Sequence in the hanging wall of the MCT (Fig 2A). Samples 24KG07 and 24KG08 are medium grained gneisses with visible gneissic banding in hand sample, and sample 24KG09 is a medium grained mylonite with sheared plagioclase clasts, showing top to the south sense of shear. Samples 24KG10 (2498m), 24KG11 (2753m), and 24KG12 (2966m) were collected in the Greater Himalayan Sequence between the MCT and the STD (Fig 2A, 2B). Samples 24KG10 and 24KG12 have a similar medium-coarse grained mylonitic fabric, whereas sample 24KG11 is a medium-coarse grained gneiss. Finally, samples

24KG05 (1434m) and 24KG06 (1540m) were collected from a fine-grained schist with local gneissic banding (24KG05) and a fine-grained interbedded quartzite and schist (24KG06) in the hanging wall of the MCT. Sample 24KG05 is a fine-grained schist with local gneissic banding, and sample 24KG06 is a medium-fine grained interbedded quartzite and schist. Sample 24KG04 was collected in the hanging wall of the Ramgarh Thrust, and it is a fine-grained schist in the Lesser Himalayan Sequence. Monazite and apatite grains were extracted following standard mineral separation procedures after Kohn et al, (2018).

Monazite Fission Track, U-Th-Pb and Trace Element Analysis

Monazite grains were hand-picked and mounted in epoxy, followed by grinding with 1000 and 2500 grit paper and lapping film. Grains were further polished in 0.3 μm alumina paste. Following monazite fission-track etching protocols outlined by Jones et al, (2019) and Nakajima et al., (2024) samples 24KG04, -05, -07, -10, -11, and –12 were etched in 6 M HCL for 60 minutes at ~90° C, and samples 24KG08 and –09 were etched in 6 M HCL for 90 minutes at ~90° C. Monazite fission-tracks were counted in crystals that were approximately oriented on their (100) face and measured using a Zeiss Axio Imager 2 microscope and Fijjontrack Image J plugin (Lang et al., 2023) at the University of Oklahoma (OU) at the Structure, Tectonics, OU Thermochronology (STOUT) laboratory.

Monazite isotopic and trace element data were collected using a Photon Machines Analyte 193 excimer laser ablation system connected to a PlasmaQuant MS Elite inductively couples plasma mass spectrometer (Shaulis et al., 2010) at the University of Houston (UH). A laser energy density of ~5.6 j/cm^2, a repetition rate of 7 hz and a spot diameter of 4 mm were used. Along with ^{235}U, ^{232}Th and $^{204-208}$Pb, major elements ^{29}Si and ^{31}P, trace elements ^{88}Sr and ^{89}Y and rare elements (REE: ^{139}La, ^{140}Ce, ^{146}Nd, ^{147}Sm, ^{153}Eu, ^{157}Gd, ^{159}Tb, ^{163}Dy, ^{165}Ho, ^{166}Er, ^{169}Tm, ^{172}Yb, and ^{175}Lu) were measured. Monazite standard 44069 was used as a primary standard for Th-Pb ratios and trace element concentrations and monazite standard 554 was used as a secondary standard to check accuracy (Grove and Mark Harrison, 1999; Liu et al., 2012). Mass concentration (X_Trace_Elements_IS) and isotope ratio (U-Pb Geochronology) determination were performed using Iolite v4 (Paton et al., 2011; Barla et al., 2023).

Monazite fission track ages were calculated using a modified laser ablation fission-track equation after (Gleadow et al., 2015; Vermeesch, 2017) using an initial track-length of 10.6 μm (Weise et al., 2009; Jones et al., 2019) and a monazite density of 5.22 g/cm^3 (Nasdala et al., 2020; Jones et al., 2023). The fission-track parent ^{238}U concentration was determined using LA-ICP-MS as described above. The ^{232}Th isotope also undergoes spontaneous fission, but this is usually not considered an issue in apatite, titanite and zircon due to the relatively low concentration and long spontaneous fission decay constant of Th. Monazite contains significant (~8.0 wt%) concentrations of Th (Rapp and Watson, 1986) however, given the relatively young rock crystallization age (Paleogene-Eocene) and the extremely long ^{232}Th spontaneous fission decay constant of 1.2 x 10-21 yr^{-1}, particularly relative to that of ^{238}U (~7.0 – 8.7 x 10 – 17 yr^{-1}; Guedes et al., (2003) we consider the influence of possible ^{232}Th tracks to be negligible (Holden and Hoffman, 1993). Due to the absence of a suitably characterized monazite fission-track standard, single-grain ages were calculated using the absolute method (Gleadow et al., 2015; Vermeesch, 2017). Monazite fission-track central ages were determined using Radialplotter (Galbraith, 2005; Vermeesch, 2009).

Apatite Fission Track, U-Pb and Trace Element Analysis

Within apatite, the damage caused by spontaneous fission is annealed on geologic timescales at temperatures typically >120°C and remain relatively stable at temperatures <60°C (e.g., Green et al., 1986; Stephenson et al., 2006). Apatite grains were mounted in epoxy, polished to reveal an internal section and etched in 5.5M HNO_3^- at 20 ± 1 °C for 20 ± 1s following the protocol of Donelick, (2005). Fission-tracks were counted and measured at the STOUT Laboratory on a Zeiss Axio Imager 2 using the Fijjiontrack ImageJ plugin for fission-track analysis (Lang et al., 2023).

Apatite ^{238}U concentrations and trace element concentrations for this study were collected using a Photon Machines Analyte 193 excimer laser ablation system connected to a PlasmaQuant MS Elite Inductively couples plasma mass spectrometer (Shaulis et al., 2010) at the University of Houston (UH). A laser energy density was ~3.9 j/cm^2, a repetition rate of 7 hz, a spot diameter of 30 mm and an ablation was run for 210 shots. Along with ^{235}U, ^{232}Th and $^{204-208}$Pb, major element ^{43}Ca, trace elements ^{88}Sr and ^{89}Y, and rare earth elements (REE: ^{139}La, ^{140}Ce, ^{146}Nd, ^{147}Sm, ^{153}Eu, ^{157}Gd, ^{159}Tb, ^{163}Dy, ^{165}Ho, ^{166}Er, ^{169}Tm, ^{172}Yb, and ^{175}Lu) were measured. Apatite standard McClure was used as a primary standard for U-Pb ratios (Schoene and Bowring, 2006), NIST612 was used as the primary standard for trace element concentrations (Barla et al., 2023) and Durango apatite (McDowell et al., 2005) was run as a secondary standard to check accuracy and perform a session-zeta correction (Vermeesch, 2017). Apatite fission-track ages were calculated using a modified fission-track equation after Hasebe et al., (2004), Gleadow et al., (2015), and Vermeesch, (2017). Durango apatite was used as a session-zeta to normalize single-grain fission-track ages and correct for instrumental drift (Vermeesch, 2017). Central ages were determined using Radialplotter (Galbraith, 2005; Vermeesch, 2009).

Results

Monazite U-Th-Pb and Trace Element Analysis

Four samples yielded monazite U-Th-Pb dates between ~ 500 and 20 Ma. Sample 24KG07 yielded a concordia age of 41.0 ± 3.3 Ma (n = 6; MSWD = 9.5; Fig 3A, Fig 4A). 24KG07 displays a steeply deepening REE pattern, yielding relatively enriched in light rare earth element (LREE) (La/Sm_{cn} = 4.65 ± 0.41), variably depleted in heavy rare earth elements (HREE; Dy/Yb_{cn} = 14.52 ± 12.36) and a relatively elevated Eu anomaly of 0.589 ± 0.087.

Sample 24KG10 yielded a concordia age of 30.6 ± 1.7 Ma (n = 29; MSWD = 1.1; Fig 3B, Fig 4B). 24KG10 displays a steeply deepening REE pattern, yielding relatively enriched in LREEs (La/Sm_{cn} = 4.45 ± 0.91) relatively depleted in HREE (Dy/Yb_{cn} = 7.57 ± 0.82) and a significant Eu anomaly of 0.08 ± 0.01.

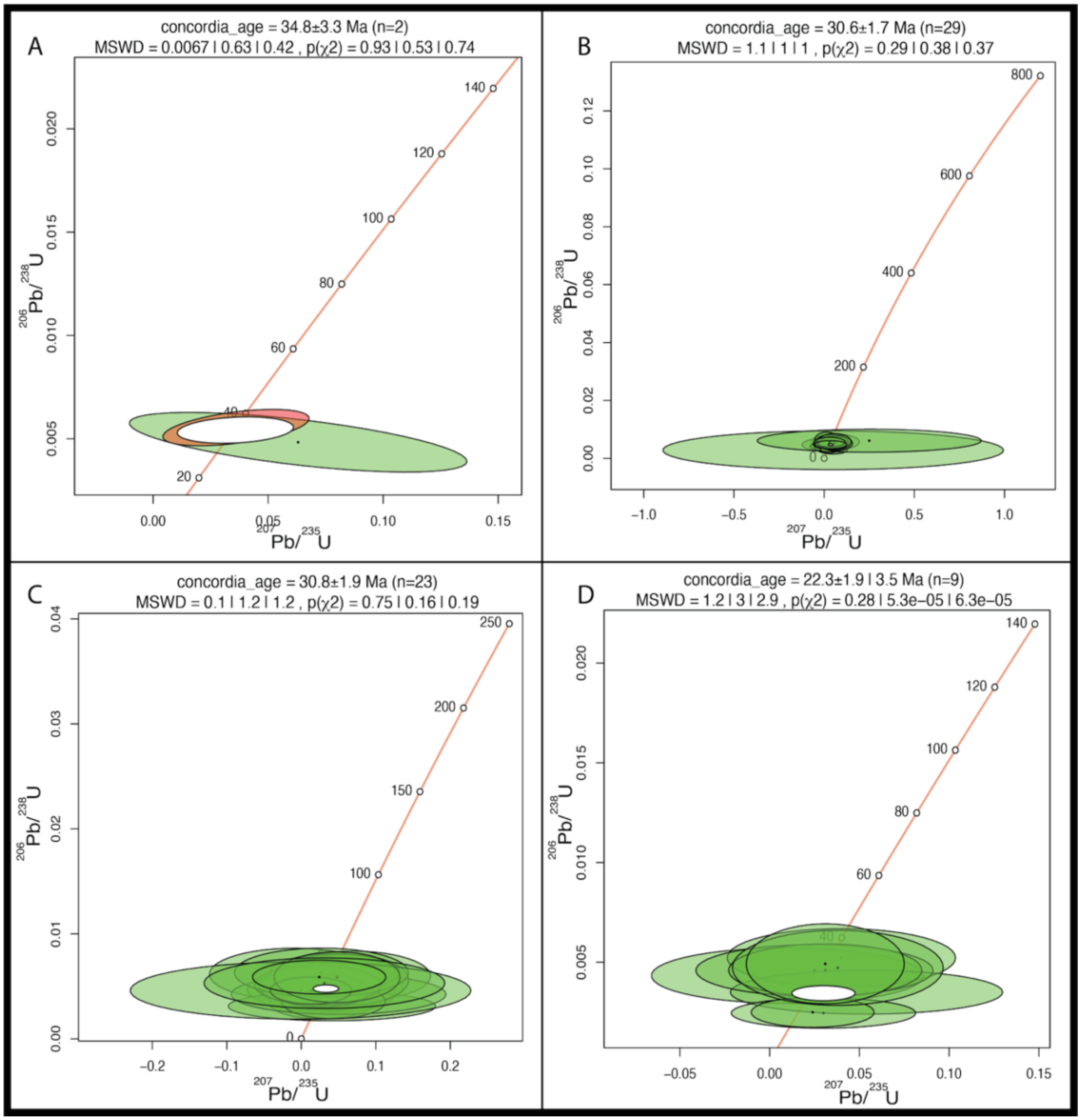

Figure 3. A) Sample 24KG07 Monazite U-Th-Pb Concordia plot.B) Sample 24KG10 Monazite U-Th-Pb Concordia plot. C) Sample 24KG11 Monazite U-Th-Pb Concordia plot. D) Sample 24KG12 Monazite U-Th-Pb Concordia plot. Figures made with IsoplotR software (Vermeesch).

Sample 24KG11 yielded a concordia age of 30.8 ± 1.9 Ma (n = 23; MSWD = 0.1; Fig 3C, Fig 4C). 24KG11 displays a steeply deepening REE pattern, yielding relatively enriched in LREE (La/Sm_{cn} = 3.99 ± 0.59), relatively depleted in HREE (Dy/Yb_{cn} = 5.33 ± 1.38) and a significant Eu anomaly of 0.073 ± 0.012.

Sample 24KG12 yielded a concordia age of 39.0 ± 1.9 Ma (n = 30; MSWD = 640; Fig 3D, Fig 4D). 24KG12 displays a steeply deepening REE pattern, yielding relatively enriched in LREE (La/Sm_{cn} = 4.48 ± 1.05), relatively depleted in HREE (Dy/Yb_{cn} = 9.96 ± 1.58) and a significant Eu anomaly of 0.072 ± 0.019.

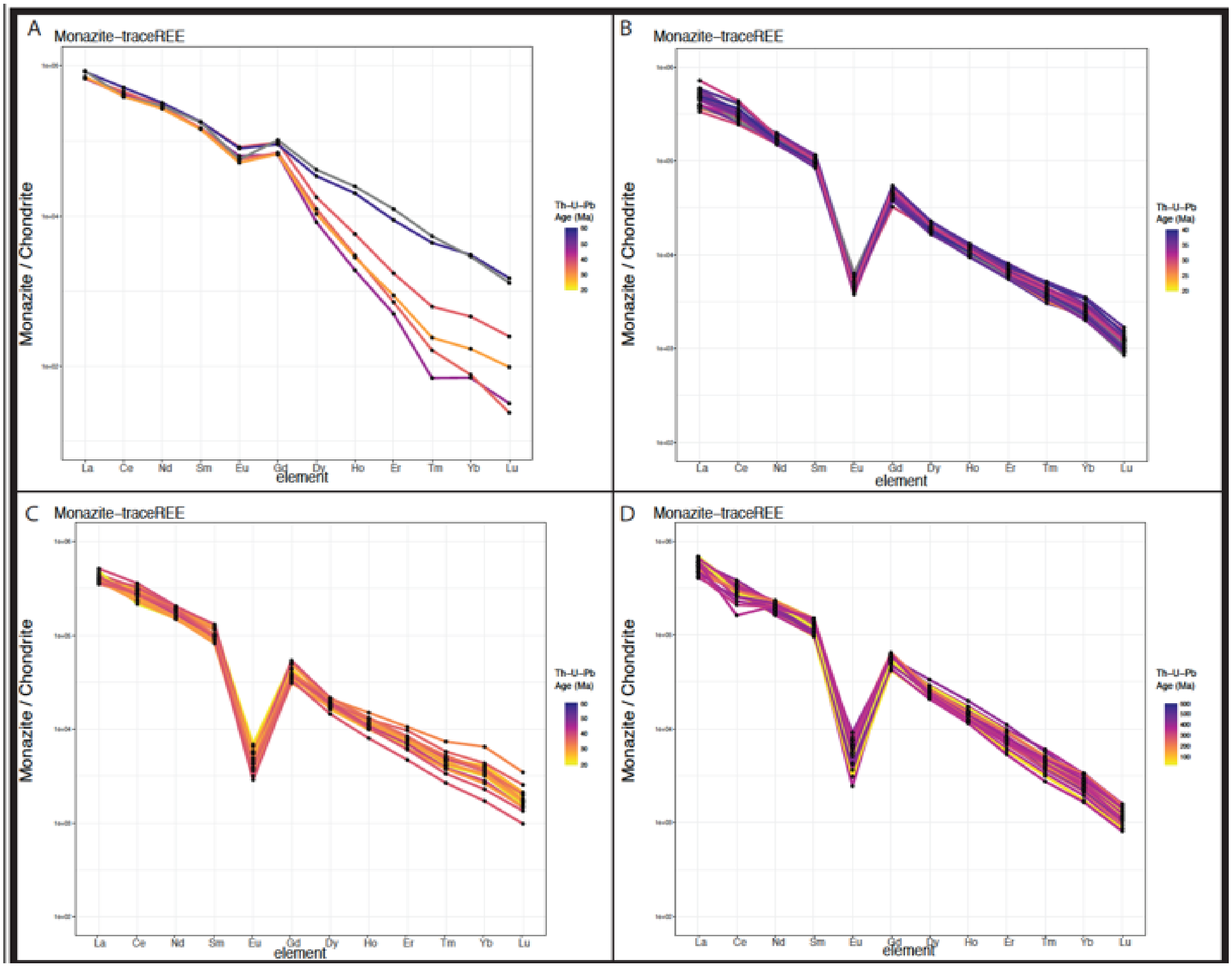

Figure 4. A) Sample 24KG07 REE spider plot plot.B) Sample 24KG10 REE spider plot. C) Sample 24KG11 REE spider plot. D) Sample 24KG12 REE spider plot. Figures made with IsoplotR software (Vermeesch, 2018).

Apatite Fission-Track Analysis

Samples 4,5,8,9,10,11, and 12 yielded anomalously low ^{238}U concentrations < 0.5 ppm. Thus, were excluded from AFT analysis as they yielded ages that were geologically unreasonably (>>100 Ma). Two samples yielded apatite with sufficient ^{238}U concentrations for AFT analysis. Sample 24KG06 yielded a central age of 9.5 ± 4.4 Ma (n = 6; Fig 5A) and a dispersion of 92%. This sample fails the χ^2 test ($P(\chi^2) = 0.0$) suggesting that there is more uncertainty than what is captured by the central age. Sample 24KG07 yielded a central age of 3.03 ± 0.44 Ma (n = 25; Fig 5B) and a relatively high dispersion of 30%. However, it passed the χ^2 test ($P(\chi^2) = 0.16$), suggesting a single population.

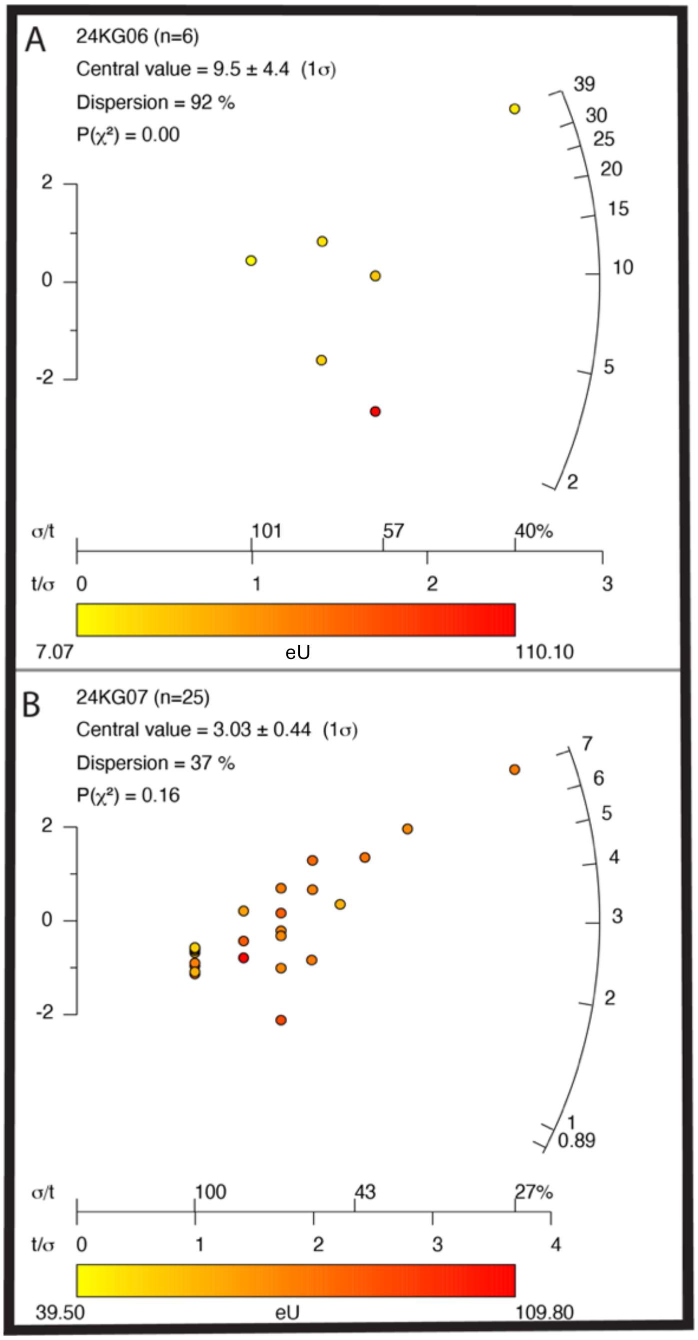

Figure 5. A) Sample 24KG06 Apatite Fission-Track radial plot. B) Sample 24KG07 Apatite Fission-Track radial plot. Figures made with RadialPlotter (Galbraith, 2005; Vermeesch, 2007). eU is effective uranium

Monazite Fission-Track Analysis

Samples 24KG12, 24KG11 and 24KG10 were collected along a vertical elevation profile and sample 24KG07 was collected at a lower elevation along the Kali Gandaki River. Sample 24KG12 (n=24) (2966 m) yielded an over-dispersed MzFT distribution (68%). Recent studies using monazite fission-track from basement rocks have observed multiple populations (e.g., (Galbraith, 2005; Vermeesch, 2009). Here, we subdivided sample 24KG12 into two populations with an older peak age of 0.336 ± 0.028 Ma (70% of the single-grain data) and a younger peak age of 0.087 ± 0.012 Ma (30% of the single-grain data). Sample 24KG10 (n = 25; 2498 m; Fig 6B) yielded single MFT central age of 0.246 ± 0.018 Ma and a dispersion value of 7.3%. Sample 24KG11 (n = 16; 2753 m; Fig 6C) yielded a single MzFT central age of 0.395 ± 0.041 Ma and a dispersion value of 19%. Sample 24KG07 (n = 5; 1830 m; Fig 6A) single MzFT central age of 0.094 ± 0.024 Ma and a dispersion value of 0%.

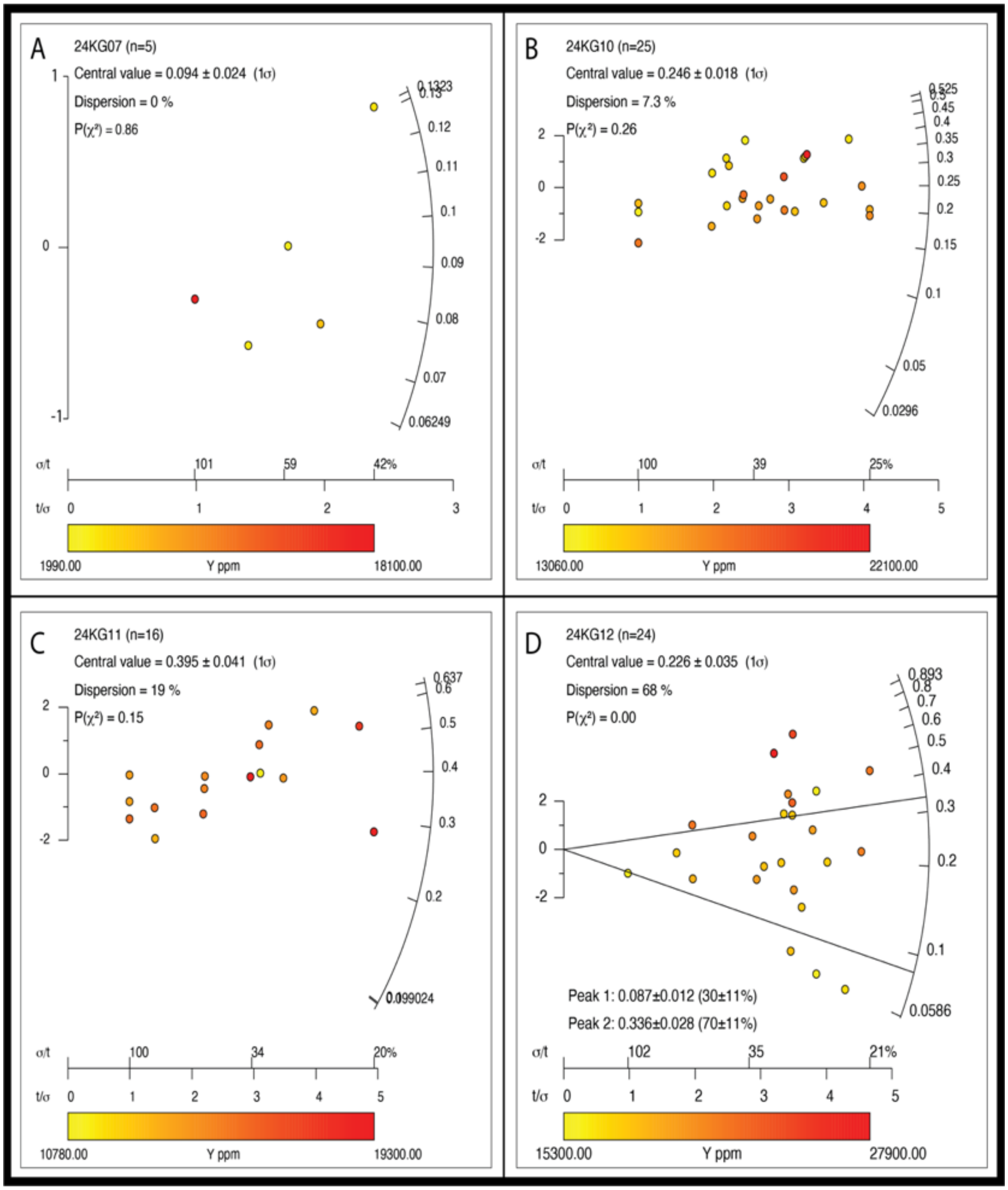

Figure 6. A) Sample 24KG07 Monazite Fission-Track radial plot. B) Sample 24KG10 Monazite Fission-Track radial plot. C) Sample 24KG11 Monazite Fission-Track radial plot. D) Sample 24KG12 Monazite Fission-Track radial plot. Peaks 1 and 2 represent two age populations. Plots made with RadialPlotter (Galbraith, 2005; Vermeesch, 2007)

Thermal History Modelling

Thermal history modeling was performed using single-grain MzFT ages and confined track lengths from this study. We used QTQt software (version 5.9.0) to determine the thermal history of samples 24KG10 and 24KG11, representative of the Kali Gandaki elevation profile. QTQt implements a Bayesian trans-dimensional Markov Chain Monte Carlo approach (Gallagher, 2012) to adequately predict time-temperature paths based on the data for a sample (Jepson et al., 2025). The model was based on two samples (24KG10, 24KG11) as part of an elevation profile (vertical separation of ~255 m between two samples) in the Kali Gandaki river valley in central Nepal (Figure 1). This combined thermal history model was run excluding He data from Pye et al., (2023), and used the Jones et al. (2022) fanning annealing model. We placed an initial temperature constrain of 80°C ± 40°C 0.7 ± 0.3 Ma based on the apatite (U-Th-Sm)/he (AHe) results from the Kali Gandaki (Pye et al., 2023; Fig 2).

Interpretation

Monazite U-Th-Pb and Trace Elements Analysis

Four monazite samples yielded U-Th-Pb ages of ~500 – 30 Ma, with two main populations, one of ~500 – 300 Ma and a second of 40-30 Ma (Fig 3). The older population, ~500 – 400 Ma signal correlates with significant Paleozoic metamorphism in the Greater Himalayan Sequence, supporting DeCelles et al., (2020) and Soucy La Roche & Godin, (2019). Whereas the younger, ~40-30 Ma signal correlates with a period of prograde metamorphism in the Greater Himalayan Sequence during the Middle Eocene. Soucy La Roche & Godin, (2019) report peak garnet-grade metamorphism in the GHS to be between 35 and 30 Ma, and the start of garnet growth at ~40 Ma (Fig 7). Therefore, this younger signal likely occurs between stage 2 and 3 of garnet growth (Soucy La Roche and Godin, 2019). Finally, several monazites yield U-Th-Pb ages between 400 Ma and 200 Ma. We suggest that these ages reflect variable overprinting of Paleozoic metamorphism by Eocene prograde metamorphic conditions.

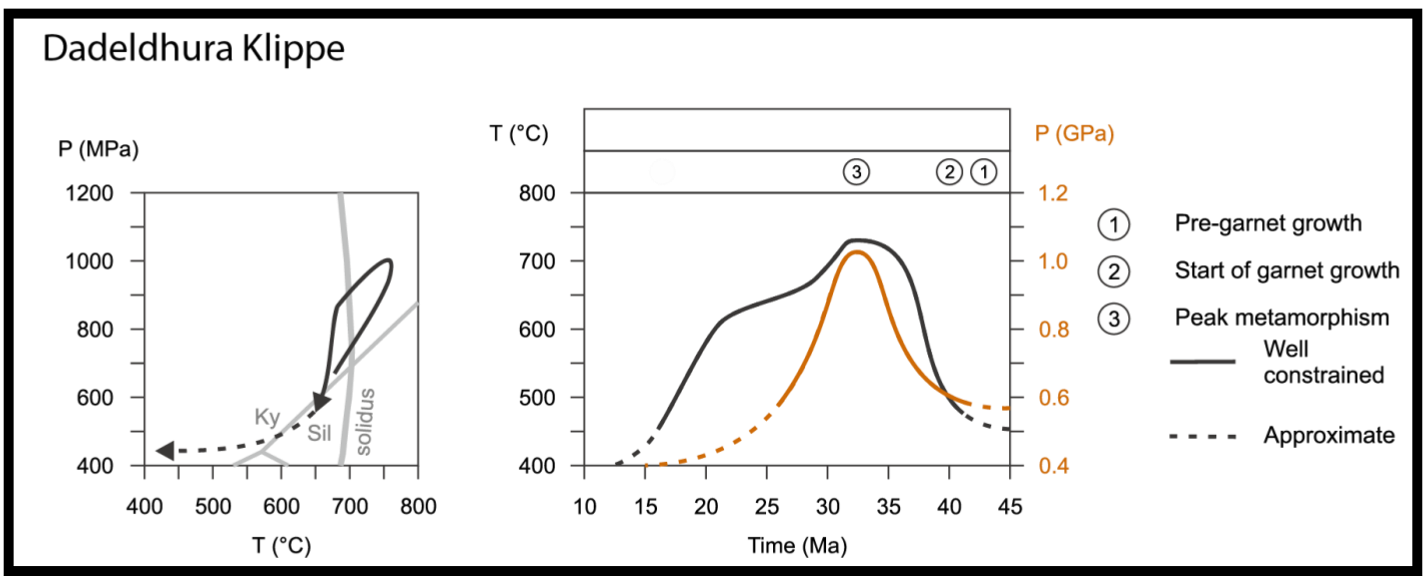

Figure 7. P-T-t diagram showing garnet growth in the Dadeldhura Klippe (Greater Himalayan Sequence). Figure modified from Soucy La Roche and Godin (2019).

Three monazite samples (24KG10, 24KG11 and 24KG12) are enriched in LREE and are depleted in HREEs. These three samples also show a major europium anomaly (e.g., ~0.08 – 0.07; Fig 4). Large Eu anomalies are typically correlated to the cogenetic growth of monazite and plagioclase (Puchelt and Emmermann, 1976). Sample 24KG07 similarly shows enriched LREE (La/Sm_{cn} = 4.65 ± 0.41), however, it yields variably depleted HREE ratio (Dy/Yb_{cn} = 14.52 ± 12.36; Fig 4). The depletion of HREEs in accessory phases (e.g., zircon and monazite) is commonly associated with cogenetic garnet growth (Rubatto et al., 2001; Warren et al., 2019). Thus, we suggest that the variable HREE depletion observed occurs as a function of monazite growth during garnet-in metamorphic conditions (Pyle, 2001; Kylander-Clark et al., 2013; Soucy La Roche and Godin, 2019).

Apatite Fission-Track Analysis

Out of the nine samples analyzed, only two (24KG06 and 24KG07) yielded AFT ages younger than the rocks corresponding crystallization age. This was due to the extremely low uranium concentrations (Donelick, 2005; Vermeesch, 2017). Sample 24KG06 yielded a central age of 9.5 Ma ± 4.4 Ma (n = 6) and a dispersion of 92% (Fig 5). These ages are within uncertainty with a previous apatite and zircon (U-Th-Sm)/He study from along the Kali Gandaki valley (Pye et al., 2023), who identified cooling ages of ~4.50 – 0.70 (Figs 2 and 8).

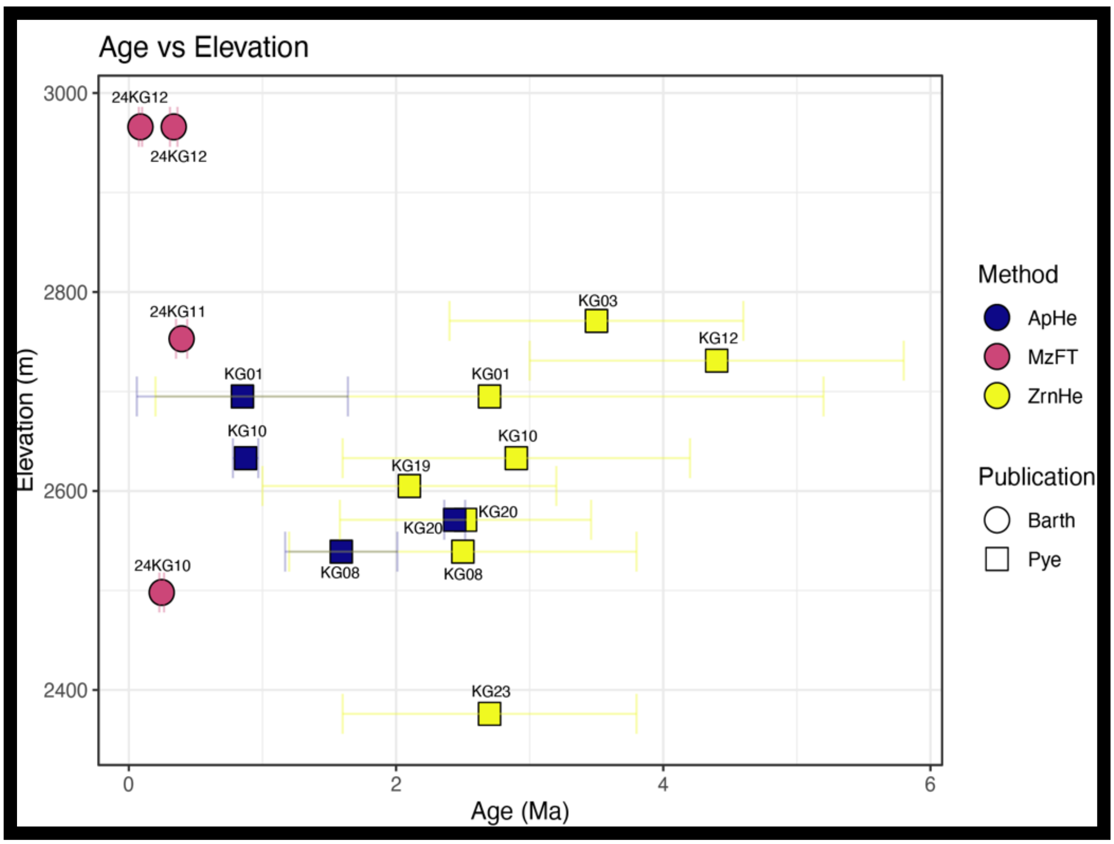

Figure 8. Age-Elevation plot including monazite fission-track(MzFT; this paper) apatite (U-Th-Sm)/He (ApHe; Pye et al., 2023) and zircon (U-Th)/He (ZrnHe; Pye et al., 2023) results. Samples from Pye et al., 2023 were collected along the Kali Gandaki river. Sample 24KG07 was removed for this plot.

In the adjacent Marsyandi River, Blythe et al., (2007) collected an extensive profile of AFT data which yielded ages of ~4-0 Ma. Sample 24KG06 was over-dispersed with one single-grain age with a U concentration above 2 ppm (e.g., Donelick, 2005; Vermeesch, 2017) which yielded an age of ~9.5 Ma. As a result of low uranium concentrations, the central age likely reflects a spurious event. However, the presence of a young grain (~3 Ma) suggests that this sample still records some processes related to upper crustal exhumation (e.g., Blythe et al., 2007).

Sample 24KG07 yielded a central age of 3.03 ± 0.44 Ma (n = 25; Fig 5) and a dispersion of 30%. This sample yielded relatively high U concentrations (i.e., 59.5 ppm) and passed the χ2 test ($P(\chi^2)$= 0.16), suggesting a single population. These data are in close agreement with the AHe results from Pye et al., (2023) in close-proximity samples from the Kali Gandaki valley (2.44± 0.078 – 0.70± 0.70 Ma) and the adjacent Blythe et al., (2007) AFT results in the adjacent Marsyandi valley (4 –0 Ma). We suggest these AFT ages correlate to a period of exhumation in the Pliocene (e.g., Pye et al., 2023).

Monazite Fission-Track Analysis

Three samples (24KG12, 24KG11 and 24KG10) were collected along an elevation profile (Δelevation = 468 m, Fig 8). The lower two samples, 24KG10 and 24KG11, yielded ages of ~0.25 and ~0.4 Ma, respectively, while the highest elevation sample, 24KG12, yielded a bimodal age population with an older population of ~0.34 Ma and a younger population of 0.087 Ma.

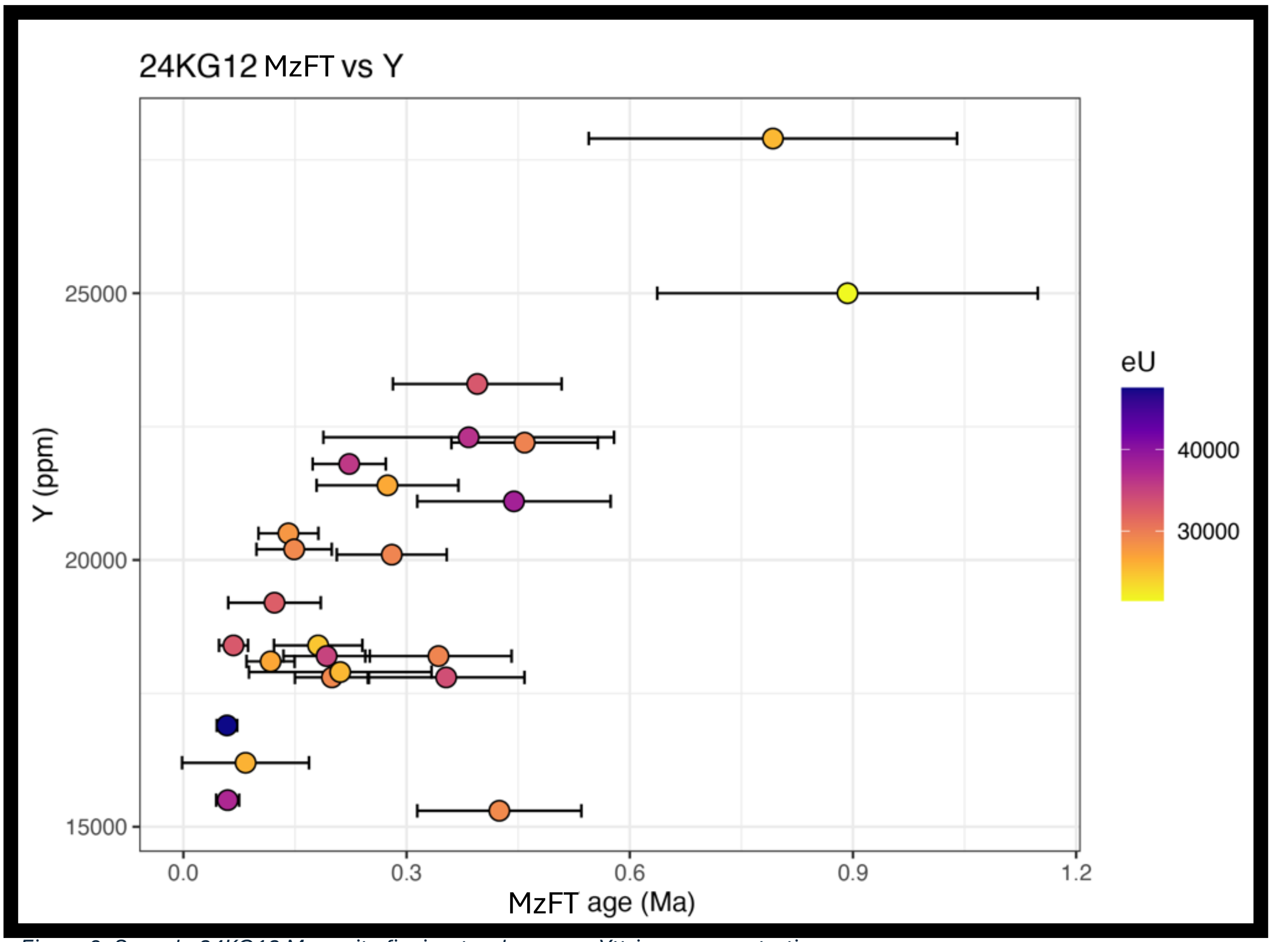

Figure 9. Sample 24KG12 Monazite fission-track ages vs Yttrium concentration.

In more well-established fission track thermochronology methods (e.g., apatite fission-track and zircon fission-track), it is unusual for an igneous or metamorphic sample to preserve multiple age populations. Over-dispersed basement samples traditionally interpreted as reflecting partial annealing of a prior cooling event (e.g.,Gleadow et al., 2002). However, AFT samples with elevated Cl concentrations have been found to correspond to higher annealing temperatures and potentially multip)ulations or cooling events (e.g., Green et al., 1986; Issler et al., 2022) In monazite, fission-track ages have been found to correlate with major and trace element geochemistry (Jones et al., 2023; Jepson et al., 2025). Jones et al., (2023) applied MzFT to four granitoid plutons in SW Japan and find multiple distinct age populations strongly correlated with eU content within the samples. In addition, Jones et al., (2023) identified that monazites with higher Si concentrations were more resistant to annealing. Similarly, Jepson et al., (2025) observes a trend where metamorphic and igneous derived monazites yield multiple age populations as defined by the yttrium concentration. Therefore, we divide 24KG12 MzFT ages

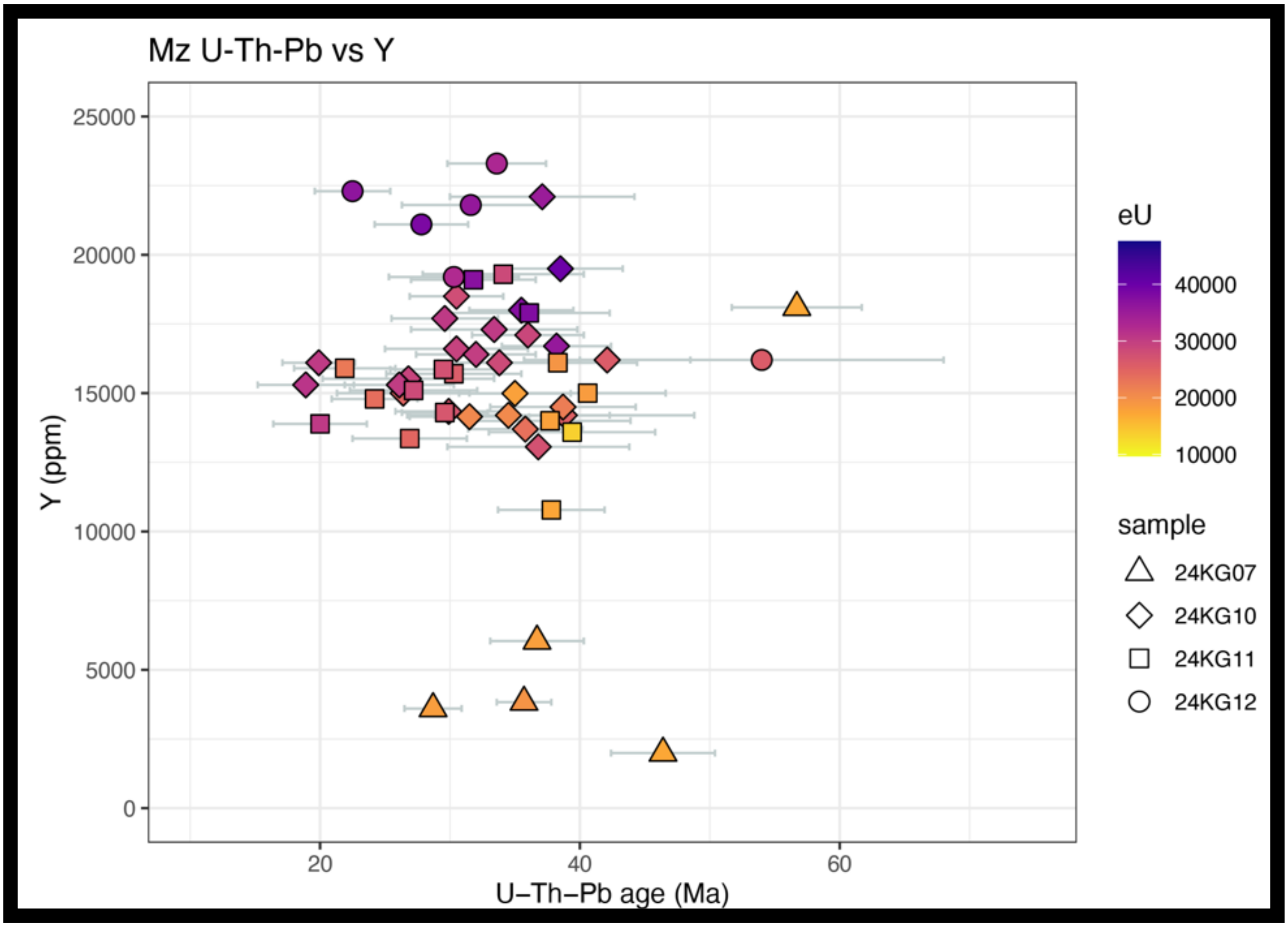

Figure 10. All monazite U-Th-Pb data vs Yttrium concentration.

based on high Y and low Y concentrations (Fig 9). We suggest that Y concentration may play a role, either as a mechanism or a proxy, for a geochemical control on annealing.

The older population of 24KG12 (0.336 Ma) is consistent with a period of relatively rapid cooling between ~0.4 - 0.2 Ma yielded from the lower elevation samples 24KG11 and 24KG10. Sample 24KG07 was collected at a lower elevation (1830 m) further down in the Kali

Gandaki valley (~12 km) and yields a single MzFT age population of ~0.09 Ma. The 0.09 Ma age is consistent with the young population (0.087 Ma) identified in 24KG12. The presence of multiple MzFT age populations as discriminated by Y within a single sample suggests that the

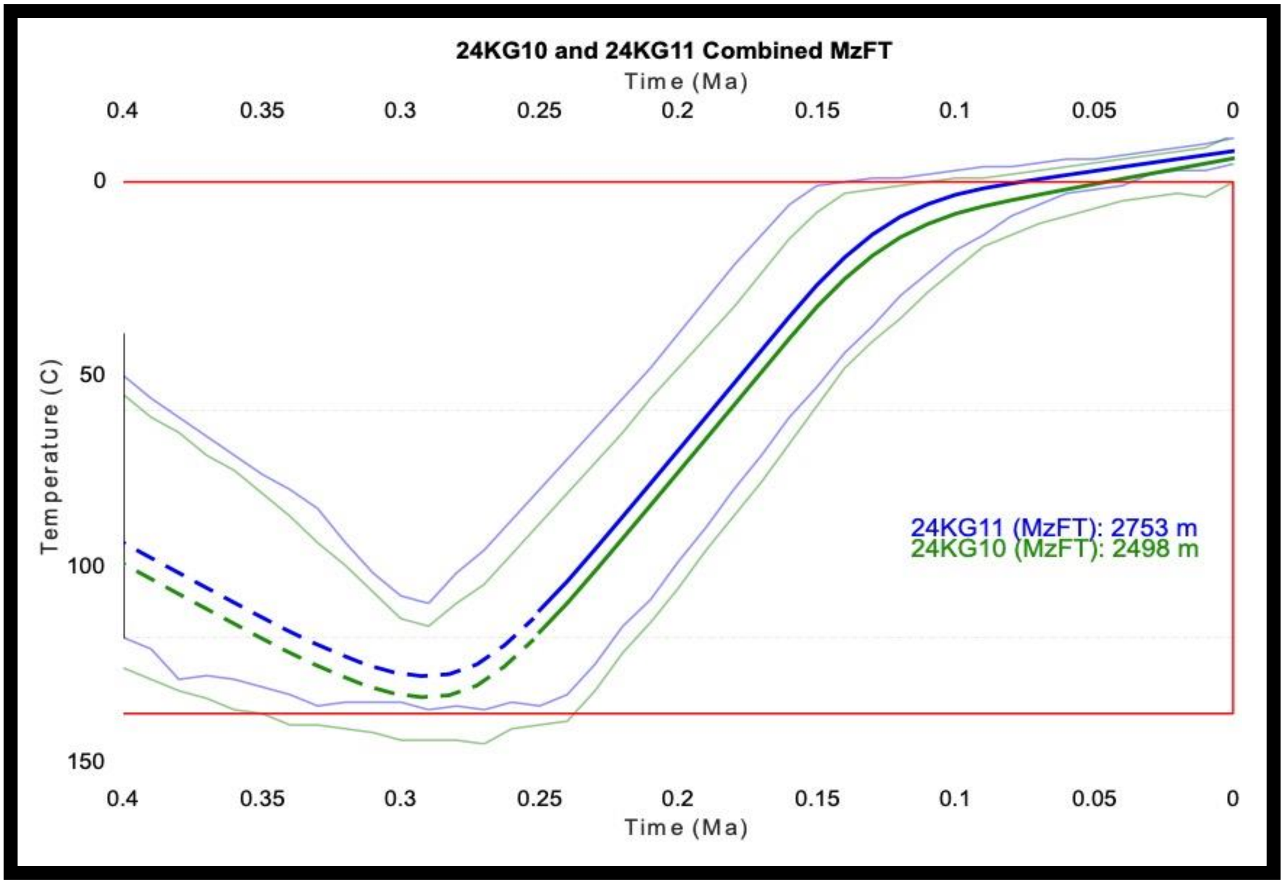

Figure 11. Thermal history model made with QTQt software (Gallagher, 2012) of samples 24KG10 and 24KG11. Dashed line represents the over-estimated initial heating produced by the model.

monazite geochemistry plays a significant control on the precise temperature required for annealing.

Thermal History Modeling

Initially, the model displays a period of heating from the initial constraints (0.7 ± 0.3 Ma, 80°C ± 40°C) to ~140°C – 100°C at 0.28 Ma (Fig. 11). This initial period of reheating is inconsistent with published data from Pye et al, (2023) which shows that these rocks cooled through the apatite partial retention zone (~80 – 40 °C) by at least 0.7 Ma. An early period of reheating would overprint these published data and even younger AHe ages. Thus, we suggest that the MzFT annealing model may be over-estimating the magnitude of heating required to anneal the MzFT system (Jones et al., 2021; Jepson et al., 2025). However, given the large range of uncertainty shown by the youngest AHe age, we cannot be certain that some degree of reheating did not occur (Pye et al., 2023). This initial heating is followed by a period of rapid cooling from ~140 – 80 °C to ~30 – 0°C between 0.25 and 0.15 Ma (Fig 11). The timing of this rapid cooling is consistent with our qualitative estimates which show 5.2 ± 0.27 mm/yr of apparent exhumation (Fig 8). Lastly, the model yields a period of slower cooling from ~30°C - - 10°C between 0.13 – 0 Ma (Fig 11). This period of cooling is consistent with the lower elevation

MzFT sample (24KG07; 1830 m) which yielded a central age of ~0.09 Ma (Fig 8 and 6a). In general, after 0.25 Ma, model adequately describes our tT predictions for the cooling history of MzFT in the sampled region.

Discussion

Paleozoic Magmatism:

We observe a minor population of ~400 Ma monazite U-Th-Pb ages preserved in sample 24KG12 (Fig 3D). The Greater Himalayan Sequence broadly consists of Neoproterozoic to Cambrian sedimentary and metasedimentary rocks (DeCelles et al., 2020). An extensive compilation of detrital zircon U-Pb ages spectra (n = 1399) from the metasedimentary rocks find that the protolith age of the GHS is likely > 500 Ma (Parrish and Hodges, 1996; Gehrels et al., 2011). Within the GHS, Cambrian to Silurian monazite and zircon U-Th-Pb ages have been reported from mylonitic orthogneisses (Catlos et al., 2002; Gehrels et al., 2011). The (meta)sedimentary GHS protoliths are interpreted to represent sediments derived from the Gondwana orogen (~570 – 480 Ma), east African orogen (~650 – 620 Ma), Grenvillian orogenic belts (~1350 – 900 Ma), and Archean-Paleoproterozoic cratons (Cawood et al., 2007; Myrow et al., 2010). The Cambrian to Silurian orthogneiss ages, however, are interpreted to represent a period of magmatic intrusion associated with convergent margin magmatism/terrane accretion along the northern margin of Gondwana (e.g., Cawood et al., 2007). Here, we suggest that our ~400 Ma monazite U-Th-Pb ages correspond to the timing of magmatic emplacement of the orthogneiss protolith.

Eocene Prograde Metamorphism:

Our Cenozoic monazite U-Th-Pb data record two age populations; one at ~40 – 30 Ma and a second at ~20 Ma. The Eocene – Oligocene monazite U-Th-Pb ages (40-30 Ma) are widely reported throughout the GHS but are typically restricted to the structurally highest sections (Corrie and Kohn, 2011; Kohn, 2014). Kohn (2014) explains this boundary with monazite geochemical and geochronologic analyses in the Modi Khola transect (east of Kali Gandaki). They determine the main phase of movement along the MCT to occur between ~20 – 15 Ma, structurally dividing the lower GHS and upper LHS (Kohn, 2014; DeCelles et al., 2020; Pye et al., 2023). Similarly, Pye et al, (2022) uses U-Th-Pb age of monazites from leucogranites in the Kali Gandaki valley to suggest slip on the STD ceased by 22 Ma. Our late Eocene ages are older than the proposed timing of the MCT and STD (DeCelles et al., 2020; Pye et al., 2022, 2023). Detrital thermochronologic and geochronologic signatures from the Dumri and Bhainskati Formations (part of the Foreland Basin Sequence) in northern Nepal yield Eocene ages of ~40 Ma, suggesting crustal growth and erosion of the Tethyan Himalayan region during this time (Najman et al., 2005; Stickroth et al., 2019; DeCelles et al., 2020). Our data support the interpretation that crustal thickening, uplift and erosion of the Tethyan Himalayan Zone adequately explains the Eocene – Oligocene signal in the GHS, and ultimately metamorphism prior to STD and MCT exhumation.

The presence of garnet in samples 24KG07, 24KG10, 24KG11 and 24KG12 suggests that the ~40-30 Ma signal represents peak and prograde metamorphism in the GHS. Similarly, Zhu and O'Nions, (1999) review the REE distribution in monazite from the Lewisian complex of NW Scotland. They find a trend in garnet growth as it effects Y and HREE concentration, where those monazite-bearing samples containing garnet yield depleted Y and HREE values, and monazite in rocks without garnet present yield higher Y and HREE (Zhu and O'Nions, 1999). Here, we find that 40 – 30 Ma ages covary with a relatively depleted HREE value (Fig 4) and a relatively depleted Y value (Figure 10). Samples 24KG10, 24KG11 and 24KG12 may reflect prograde metamorphism, given their relatively high HREE and Y values. However, 24KG07 yields relatively enriched HREE and Y (Fig 10.) Thus, we suggest that there was cogenetic growth of garnet and monazite in sample 24KG07, and all four GHS samples grew during prograde to peak metamorphic conditions from 40 – 30 Ma (Zhu and O'Nions, 1999; Soucy La Roche and Godin, 2019).

Miocene Metamorphism:

The youngest monazite U-Th-Pb ages are Miocene (~20 Ma; Fig 3). Miocene metamorphism (~20 Ma) is well documented throughout the Himalaya, suggested to represent retrograde metamorphism due to exhumation along both the MCT and STD (Catlos et al., 2002; Corrie and Kohn, 2011; Kohn, 2014; Pye et al., 2022). Corrie and Kohn, (2011) provide evidence for initial cooling of the MCT at ~22 Ma, most notably that GHS samples taken along the Modi Khola at the MCT record late prograde monazite growth at 23 – 21 Ma, and cooling from 20 – 16 Ma. Similarly, Pye et al, (2022) suggests that activity on the STD continued from the late Oligocene into the middle Miocene (22.5 Ma – 14.8 Ma), determined from monazite U-Th-Pb in the Kali Gandaki valley. These U-Th-Pb ages are likely a result of Miocene N-S extension on the STD, supported by Pye et al, (2022).

Pliocene - Pleistocene Exhumation:

Our study area is dominated by three major structures; the RT, MCT and the STD (DeCelles et al., 2020; Fig 1A). The MCT is reported to begin activity at ~20 Ma (detrital muscovite $^{40}Ar/^{39}Ar$, basement muscovite $^{40}Ar/^{39}Ar$; Hodges et al., 1996; DeCelles et al., 2001; Robinson et al., 2006). The RT is reported to begin activity at ~14 Ma (Monazite U-Th-Pb, white mica $^{40}Ar/^{39}Ar$; Robinson et al., 2006; Braden et al., 2017; DeCelles et al., 2020). Together, the MCT and the RT caused considerable thickening and associated exhumation of the Himalaya. Exhumation along the MCT and RT is coeval with ductile slip along the STD. The STD was active from ~22 to as young as ~12 Ma as recorded through monazite U-Th-Pb from leucogranite bodies and muscovite Ar-Ar dating of mylonite (Pye et al., 2022). The STD accommodated significant N-S extension in the Himalaya and caused the development of a mylonite within the GHS (Pye et al., 2022). Despite the extensive Miocene (~22 – 12 Ma) deformation and exhumation accommodated along these structures, established low-temperature thermochronology methods (~250 – 40°C) yield ages which are consistently far younger (<10 Myr) than the corresponding timing of movement along each structure respectively. Published data from the Kali Gandaki and adjacent valleys correlate with our AFT results (24KG07; 3.03 ± 0.44 Ma), including AFT ages from ~3.8 – 0 Ma, AHe ages from 0.9-0.3 Ma (Marsyandi drainage; Blythe et al., 2007), AHe ages from 2.4 – 0.5 Ma (Kali Gandaki; Pye et al., 2023), and AFT ages from 14.3 – 6.7 Ma (Tila River; Sherpa et al., 2022). Based on the widespread preservation of Pliocene cooling ages, we suggest that a minimum estimate of ~10 km of exhumation would be required to remove thermochronological ages associated with fault movement along the STD, MCT, and RT. This suggests that exhumation in this region of the Himalaya is dominated by surface processes, rather than directly related to structural deformation during initial fault activity.

Pliocene – Pleistocene AHe ages (~2.4 – 0.5 Ma) from the northern Kali Gandaki valley presented by Pye et al, (2023) are interpreted to be a result of topographic changes due to basal ramp and duplex activity over the Main Himalayan Thrust (MHT) in the late Cenozoic (DeCelles et al., 2001; Robert et al., 2009; Ghoshal et al., 2023; Pye et al., 2023) or major climatic shifts in South and East Asia, including the intensification of the East Asian winter monsoon. Both hypotheses can be used to explain a significant increase in exhumation rate (1.5 mm/yr) in the Pliocene (Pye et al., 2023). Similarly, Blythe et al, (2007) collected a series of AFT ages from along the adjacent Marsyandi drainage, which range from >3.8 – 0 Ma. They generally infer this recent exhumation to be from increased activity along the MCT during the last ~1 Ma, or a change in climatic conditions (e.g., glacial-interglacial shift). However, they see no correlation between present day precipitation and increased Pleistocene exhumation because, despite the drastic northward decrease in monsoonal rainfall in the Himalayas, they find no major decrease in exhumation throughout their transects (Blythe et al., 2007). Finally, Sherpa et al, (2022) obtained a series of Miocene – Pliocene AFT ages (15 – 7 Ma) along the Tila River, a drainage west of the Kali Gandaki. They suggest that activity on the Ramgarh thrust in the late Miocene drove LHS uplift, and increase the rate of incision on the Tila River, removing surface rock (Sherpa et al., 2022). Localized basal ramp uplift, major monsoonal shifts, renewed activity of the MCT or increased river incision are all hypothesis that may explain our AFT age of ~3 Ma, as they are all capable of producing Miocene to Pliocene exhumation ages.

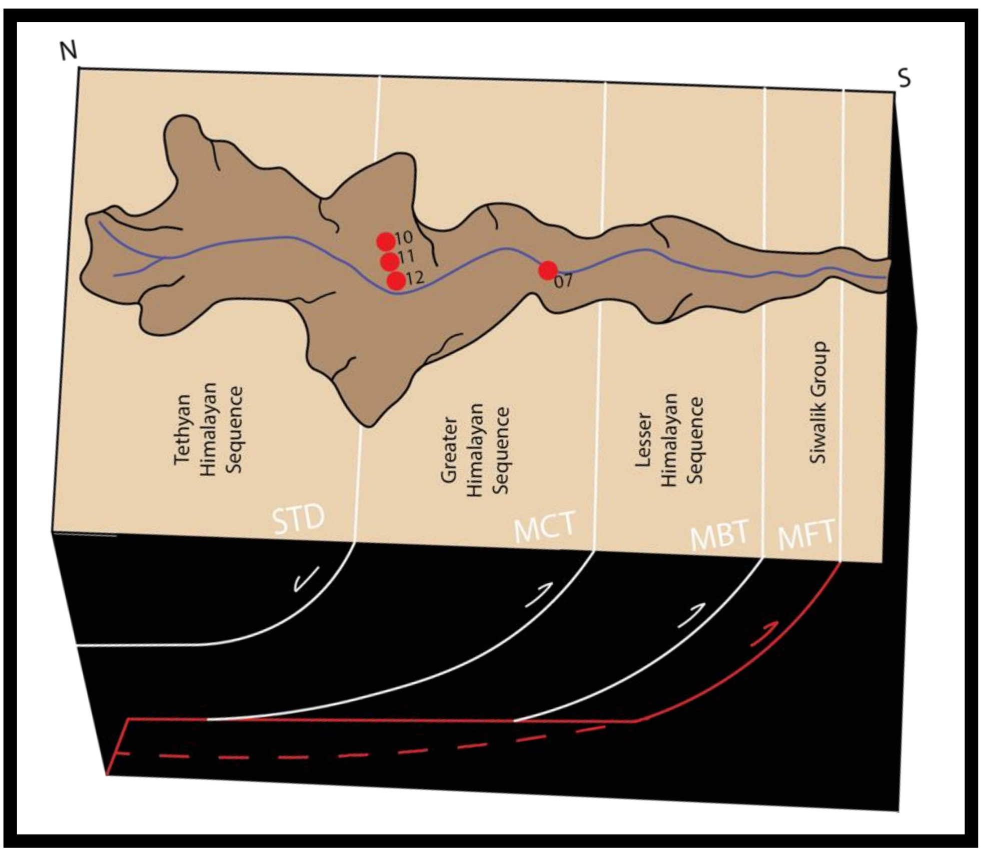

Figure 12. Schematic tectonic model of the Kali Gandaki. Red shows the active basal MFT at 280

Late Pleistocene

We sampled along the Kali Gandaki valley in an elevation profile across ~500 m, yielding MzFT ages of ~0.4-0.2 Ma. Laboratory analysis of MzFT annealing identified a broad window of annealing temperatures (~140- -70 °C; Weise et al., 2009; Jones et al., 2022). However, field-based studies suggest that MzFT ages more reasonably record to temperatures of <50 – 25 °C corresponding to exhumation in the upper 1 – 2 km of the crust (Jones et al., 2022; Jepson et al., 2025). The higher elevation sample (24KG12) is over-dispersed and therefore divided into two populations based on Y concentration of < ~20000 ppm and > ~20000 ppm (Fig 6D). The lower samples (24KG11 and 24KG10) both pass the $P(\chi^2)$ test and yield cooling ages of 0.39 and 0.25, respectively. Combined with the oldest population of 24KG12 (0.34 Ma) our MzFT data suggest a period of rapid cooling at ~0.4 – 0.2 Ma. As samples were collected across an elevation of 468 m with a relatively short horizontal separation, we leverage the age-elevation trend to produce an apparent exhumation rate (Fitzgerald et al., 1995; Gallagher, 2005). We calculate an apparent exhumation rate of 5.2 ± 0.27 mm/yr from ~0.4 – 0.2 Ma. This period of rapid exhumation is consistent with thermal history model for samples 24KG10 and 24KG11, which show a single period of rapid cooling at 0.4 – 0.2 Ma (Fig 11).

An apparent exhumation rate of ~5 mm/yr is relatively high when compared to other exhumation rates in the area, including 1.5 mm/yr since ~3 Ma in the Kali Gandaki (AHe; Pye et al., 2023) and 1.5 mm/yr from 2 – 0.8 Ma in the Marsyandi catchment (AFT; Blythe et al., 2007). Our primary hypothesis for rapid exhumation between 0.4 Ma and 0.2 Ma is activity along the MFT. Significant climate fluctuations (monsoon, glacial cycles, etc.), increased river incision, and movement of the MCT may be valuable evidence for relatively young exhumation along the Kali Gandaki. However, there has been a reported mean exhumation rate for Sub-Himalayan samples along the MFT of 6.2 mm/yr over the past ~280 k.y., implying that there has been movement along the MFT since ≤ 280 (Bouscary et al., 2024). The timing of movement along the MFT is consistent with our exhumation rate and MzFT age of the primary elevation profile (5.2 mm/yr; ~0.4-0.2 Ma), suggesting that the MFT was carrying the GHS northward since the middle Pleistocene (Fig. 12). Further, geophysical images of Himalayan subsurface structures suggest that the MFT is forming a duplex beneath the central Himalaya (~100 km north of the MFT; Lindsey et al., 2018). Thus, we suggest that the duplex is causing topographic uplift at 0.4 – 0.2 Ma which, coupled with incision by the Kali Gandaki, is exhuming our samples through the upper ~1 – 2 km of the crust (Fig. 12). Our lowest elevation sample, 24KG07, has a MzFT central age of ~0.09 Ma, and was collected outside of the primary elevation profile. We correlate this age with the younger population of 24KG12 (~0.09 Ma), proving that within the Kali Gandaki drainage, MzFT age decreases with elevation. The ~0.09 Ma MzFT ages are consistent with thermal history modelling which suggest continued cooling between 0.13 – 0 Ma (Fig. 11). Sherpa et al, (2022) explains that in order for rock uplift to coincide with progressive strike-perpendicular erosion in a drainage, higher elevation samples would yield relatively older ages. Based on our MzFT results, we suggest a relatively synchronous relationship between basal movement along the MFT and incision of the Kali Gandaki drainage since the Pliocene.

Conclusion

We present AFT, Mz U-Th-Pb and MFT data to interpret thrust activity and surface incision relationships in the Kali Gandaki valley in central Nepal. ~500-30 Ma Mz U-Th-Pb ages represent two metamorphic events in the Greater Himalayan Sequence during the Paleozoic (~500-400 Ma) and Eocene (~40-30 Ma) and Miocene (~20 Ma). HREE analysis suggests cogenetic growth of garnet and monazite in these samples. AFT results represent a period of exhumation in the Pliocene, supported by published literature in adjacent drainages. Lastly, MzFT analysis yields ages of 0.4 – 0.2 Ma, while 24KG12 yielded a bimodal age population with an older population of 0.34 Ma and a younger population of 0.087 Ma, as defined by Y concentrations. We propose these relatively young MzFT to represent ~280 k.y. movement along the basal Main Frontal Thrust during the continuous sculpting of the Kali Gandaki. MzFT allows for new opportunities to accurately explain modern surface processes and subsurface mechanisms from the upper 1-2 km of the crust.

References

Barla, A., Triantafyllou, A., Ducea, M.N., Jepson, G., McClelland, W., Giesler, D., Gehrels, G.E., and Fellah, C., 2023, A systematic evaluation of titanite reference materials for optimizing trace element and U Pb analysis by LA-ICP-MS: Chemical Geology, v. 636, p. 121635, doi:10.1016/j.chemgeo.2023.121635.

Beaumont, C., Jamieson, R.A., Nguyen, M.H., and Lee, B., 2001, Himalayan tectonics explained by extrusion of a low-viscosity crustal channel coupled to focused surface denudation: Nature, v. 414, p. 738–742, doi:10.1038/414738a.

Blythe, A.E., Burbank, D.W., Carter, A., Schmidt, K., and Putkonen, J., 2007, Plio-Quaternary exhumation history of the central Nepalese Himalaya: 1. Apatite and zircon fission track and apatite [U-Th]/He analyses: Tectonics, v. 26, p. 2006TC001990, doi:10.1029/2006TC001990.

Bouscary, C., King, G.E., Grujic, D., Lavé, J., Almeida, R., Hetényi, G., and Herman, F., 2024, Sustained deformation across the Sub-Himalayas since 200 ka: Geology, v. 52, p. 72–76, doi:10.1130/G51656.1.

Braden, Z., Godin, L., and Cottle, J.M., 2017, Segmentation and rejuvenation of the Greater Himalayan sequence in western Nepal revealed by in situ U–Th/Pb monazite petrochronology: Lithos, v. 284–285, p. 751–765, doi:10.1016/j.lithos.2017.04.023.

Braun, J., Van der Beek, P. and Batt, G., 2006. Quantitative thermochronology: numerical methods for the interpretation of thermochronological data. Cambridge University Press.

Burbank, D.W., Blythe, A.E., Putkonen, J., Pratt-Sitaula, B., Gabet, E., Oskin, M., Barros, A., and Ojha, T.P., 2003, Decoupling of erosion and precipitation in the Himalayas: Nature, v. 426, p. 652–655, doi:10.1038/nature02187.

Catlos, E.J., Harrison, T.M., Manning, C.E., Grove, M., Rai, S.M., Hubbard, M.S., and Upreti, B.N., 2002, Records of the evolution of the Himalayan orogen from in situ Th–Pb ion microprobe dating of monazite: Eastern Nepal and western Garhwal: Journal of Asian Earth Sciences, v. 20, p. 459–479, doi:10.1016/S1367-9120(01)00039-6.

Cawood, P.A., Johnson, M.R.W., and Nemchin, A.A., 2007, Early Palaeozoic orogenesis along the Indian margin of Gondwana: Tectonic response to Gondwana assembly: Earth and Planetary Science Letters, v. 255, p. 70–84, doi:10.1016/j.epsl.2006.12.006.

Corrie, S.L., and Kohn, M.J., 2011, Metamorphic history of the central Himalaya, Annapurna region, Nepal, and implications for tectonic models: Geological Society of America Bulletin, v. 123, p. 1863–1879, doi:10.1130/B30376.1.

DeCelles, P.G., Carrapa, B., Ojha, T.P., Gehrels, G.E., and Collins, D., 2020, Structural and Thermal Evolution of the Himalayan Thrust Belt in Midwestern Nepal, in Structural and Thermal Evolution of the Himalayan Thrust Belt in Midwestern Nepal, Geological Society of America, p. 1–79, doi:10.1130/2020.2547(01).

DeCelles, P.G., Kapp, P., Gehrels, G.E., and Ding, L., 2014, Paleocene-Eocene foreland basin evolution in the Himalaya of southern Tibet and Nepal: Implications for the age of initial India-Asia collision: Tectonics, v. 33, p. 824–849, doi:10.1002/2014TC003522.

DeCelles, P.G., Robinson, D.M., Quade, J., Ojha, T.P., Garzione, C.N., Copeland, P., and Upreti, B.N., 2001, Stratigraphy, structure, and tectonic evolution of the Himalayan fold-thrust belt in western Nepal: Tectonics, v. 20, p. 487–509, doi:10.1029/2000TC001226.

Donelick, R.A., 2005, Apatite Fission-Track Analysis: Reviews in Mineralogy and Geochemistry, v. 58, p. 49–94, doi:10.2138/rmg.2005.58.3.

Fitzgerald, P.G., Sorkhabi, R.B., Redfield, T.F., and Stump, E., 1995, Uplift and denudation of the central Alaska Range: A case study in the use of apatite fission track thermochronology to determine absolute uplift parameters: Journal of Geophysical Research: Solid Earth, v. 100, p. 20175–20191, doi:10.1029/95JB02150.

Gaetani, M. and Garzanti, E., 1991, Multicyclic history of the northern India continental margin (northwestern Himalaya). AAPG bulletin, 75(9), pp.1427-1446, doi.org/10.1306/0C9B2957-1710-11D7-8645000102C1865D

Galbraith, R. F., 2005, Statistics for fission track analysis. Chapman and Hall/CRC.Gallagher, K., 2005, Exploiting 3D Spatial Sampling in Inverse Modeling of Thermochronological Data: Reviews in Mineralogy and Geochemistry, v. 58, p. 375–387, doi:10.2138/rmg.2005.58.14.

Gallagher, K., 2012, Transdimensional inverse thermal history modeling for quantitative thermochronology: Journal of Geophysical Research: Solid Earth, v. 117, p. 2011JB008825, doi:10.1029/2011JB008825.

Garzanti, E., 1999, Stratigraphy and sedimentary history of the Nepal Tethys Himalaya passive margin: Journal of Asian Earth Sciences, v. 17, p. 805–827, doi:10.1016/S1367-9120(99)00017-6.

Gehrels, G. et al., 2011, Detrital zircon geochronology of pre-Tertiary strata in the Tibetan-Himalayan orogen: Tectonics, v. 30, p. 2011TC002868, doi:10.1029/2011TC002868.

Ghoshal, S., McQuarrie, N., Huntington, K.W., Robinson, D.M., and Ehlers, T.A., 2023, Testing erosional and kinematic drivers of exhumation in the central Himalaya: Earth and Planetary Science Letters, v. 609, p. 118087, doi:10.1016/j.epsl.2023.118087.

Gleadow, A.J.W., Belton, D.X., Kohn, B.P., and Brown, R.W., 2002, Fission Track Dating of Phosphate Minerals and the Thermochronology of Apatite: Reviews in Mineralogy and Geochemistry, v. 48, p. 579–630, doi:10.2138/rmg.2002.48.16.

Gleadow, A., Harrison, M., Kohn, B., Lugo-Zazueta, R., and Phillips, D., 2015, The Fish Canyon Tuff: A new look at an old low-temperature thermochronology standard: Earth and Planetary Science Letters, v. 424, p. 95–108, doi:10.1016/j.epsl.2015.05.003.

Green, P.F., Duddy, I.R., Gleadow, A.J.W., Tingate, P.R. and Laslett, G.M., 1986. Thermal annealing of fission tracks in apatite: 1. A qualitative description. Chemical Geology: Isotope Geoscience Section, 59, pp.237-253, doi.org/10.1016/0168-9622(86)90074-6

Grove, M., and Mark Harrison, T., 1999, Monazite Th-Pb age depth profiling: Geology, v. 27, p. 487, doi:10.1130/0091-7613(1999)027<0487:MTPADP>2.3.CO;2.

Guedes, S., Hadler, J.C.N., Sarkis, J.E.S., Oliveira, K.M.G., Kakazu, M.H., Iunes, P.J., Saiki, M., Tello, C.A.S., and Paulo, S.R., 2003, Spontaneous-fission decay constant of 238U measured by nuclear track techniques without neutron irradiation: Journal of Radioanalytical and Nuclear Chemistry, v. 258, p. 117–122, doi:10.1023/A:1026218411554.

Hasebe, N., Barbarand, J., Jarvis, K., Carter, A., and Hurford, A.J., 2004, Apatite fission-track chronometry using laser ablation ICP-MS: Chemical Geology, v. 207, p. 135–145, doi:10.1016/j.chemgeo.2004.01.007.

Hodges, K.V., 2000, OVERVIEW Tectonics of the Himalaya and southern Tibet from two perspectives: Geological Society of America Bulletin,.

Hodges, K.V., Parrish, R.R., and Searle, M.P., 1996, Tectonic evolution of the central Annapurna Range, Nepalese Himalayas: Tectonics, v. 15, p. 1264–1291, doi:10.1029/96TC01791.

Holden, N.E., and Hoffman, D.C., 1993, Spontaneous fission half-lives for ground state nuclides: BNL--49328, CONF-9308148--8, 10185333, BNL--49328, CONF-9308148--8, 10185333 p., doi:10.2172/10185333.

Issler, D.R., McDannell, K.T., O'Sullivan, P.B., and Lane, L.S., 2022, Simulating sedimentary burial cycles – Part 2: Elemental-based multikinetic apatite fission-track interpretation and modelling techniques illustrated using examples from northern Yukon: Geochronology, v. 4, p. 373–397, doi:10.5194/gchron-4-373-2022.

Jepson, G., Carrapa, B., Jones, S., Kohn, B. P., Gleadow, A. J., George, S. W., Howlett, C, J., Gallagher, K., Frickenstein, A, N., Gehrels, G., & Triantafyllou, A. (2025). An assessment of monazite fission-track thermochronology as a proxy for low-magnitude cooling, Catalina-Rincon Metamorphic Core Complex, AZ, USA. Geochemistry, Geophysics, Geosystems, 26(4), e2024GC011881.

Jones, S., Gleadow, A., and Kohn, B., 2021, Thermal annealing of implanted252 Cf fission tracks in monazite: Geochronology, v. 3, p. 89–102, doi:10.5194/gchron-3-89-2021.

Jones, S., Gleadow, A., Kohn, B., and Reddy, S.M., 2019, Etching of fission tracks in monazite: An experimental study: Terra Nova, v. 31, p. 179–188, doi:10.1111/ter.12382.

Jones, S., Kohn, B., and Gleadow, A., 2022, Etching of fission tracks in monazite: Further evidence from optical and focused ion beam scanning electron microscopy: American Mineralogist, v. 107, p. 1065–1073, doi:10.2138/am-2022-8002.

Jones, S., Kohn, B., Gleadow, A., Skrzypek, E., and Tagami, T., 2023, Low-temperature thermochronology of Ryoke belt granitoids, SW Japan: New insights into the recent cooling history from monazite fission-track dating: Tectonophysics, v. 864, p. 229998, doi:10.1016/j.tecto.2023.229998.

Kapp, P., and DeCelles, P.G., 2019, Mesozoic–Cenozoic geological evolution of the Himalayan-Tibetan orogen and working tectonic hypotheses: American Journal of Science, v. 319, p. 159–254, doi:10.2475/03.2019.01.

Kellett, D.A., Cottle, J.M., and Larson, K.P., 2019, The South Tibetan Detachment System: history, advances, definition and future directions: Geological Society, London, Special Publications, v. 483, p. 377–400, doi:10.1144/SP483.2.

Kohn, M.J., 2014, Himalayan Metamorphism and Its Tectonic Implications: Annual Review of Earth and Planetary Sciences, v. 42, p. 381–419, doi:10.1146/annurev-earth-060313-055005.

Kohn, B., Chung, L., & Gleadow, A. (2018). Fission-track analysis: field collection, sample preparation and data acquisition. In Fission-track thermochronology and its application to geology (pp. 25-48). Cham: Springer International Publishing.

Kylander-Clark, A.R.C., Hacker, B.R., and Cottle, J.M., 2013, Laser-ablation split-stream ICP petrochronology: Chemical Geology, v. 345, p. 99–112, doi:10.1016/j.chemgeo.2013.02.019.

Lang, A. et al., 2023, Mapping high-grade glioma immune infiltration to 5-ALA fluorescence levels: TCGA data computation, classical histology, and digital image analysis: Journal of Neuro-Oncology, v. 164, p. 211–220, doi:10.1007/s11060-023-04406-3.

Lavé, J., and Avouac, J.P., 2001, Fluvial incision and tectonic uplift across the Himalayas of central Nepal: Journal of Geophysical Research: Solid Earth, v. 106, p. 26561–26591, doi:10.1029/2001JB000359.

Lindsey, E.O., Almeida, R., Mallick, R., Hubbard, J., Bradley, K., Tsang, L.L.H., Liu, Y., Burgmann, R., and Hill, E.M., 2018, Structural Control on Downdip Locking Extent of the Himalayan Megathrust: Journal of Geophysical Research: Solid Earth, v. 123, p. 5265–5278, doi:10.1029/2018JB015868.

Liu, Z.-C., Wu, F.-Y., Yang, Y.-H., Yang, J.-H., and Wilde, S.A., 2012, Neodymium isotopic compositions of the standard monazites used in U Th Pb geochronology: Chemical Geology, v. 334, p. 221–239, doi:10.1016/j.chemgeo.2012.09.034.

Long, S.P., McQuarrie, N., Tobgay, T., Coutand, I., Cooper, F.J., Reiners, P.W., Wartho, J., and Hodges, K.V., 2012, Variable shortening rates in the eastern Himalayan thrust belt, Bhutan: Insights from multiple thermochronologic and geochronologic data sets tied to kinematic reconstructions: Tectonics, v. 31, p. 2012TC003155, doi:10.1029/2012TC003155.

McDowell, F.W., McIntosh, W.C., and Farley, K.A., 2005, A precise 40Ar–39Ar reference age for the Durango apatite (U–Th)/He and fission-track dating standard: Chemical Geology, v. 214, p. 249–263, doi:10.1016/j.chemgeo.2004.10.002.

Molnar, P., and England, P., 1990, Late Cenozoic uplift of mountain ranges and global climate change: chicken or egg? Nature, v. 346, p. 29–34, doi:10.1038/346029a0.

Myrow, P.M., Hughes, N.C., Goodge, J.W., Fanning, C.M., Williams, I.S., Peng, S., Bhargava, O.N., Parcha, S.K., and Pogue, K.R., 2010, Extraordinary transport and mixing of sediment across Himalayan central Gondwana during the Cambrian-Ordovician: Geological Society of America Bulletin, v. 122, p. 1660–1670, doi:10.1130/B30123.1.

Naeser, C.W., 1967, THE USE OF APATITE AND SPHENE FOR FISSION TRACK AGE DETERMINATIONS: Geological Society of America Bulletin, v. 78, p. 1523, doi:10.1130/0016-7606(1967)78[1523:TUOAAS]2.0.CO;2.

Naeser, C.W., and Fleischer, R.L., 1975, Age of the apatite at Cerro de Mercado, Mexico: A problem for fission-track annealing corrections: Geophysical Research Letters, v. 2, p. 67–70, doi:10.1029/GL002i002p00067.

Najman, Y., Carter, A., Oliver, G., and Garzanti, E., 2005, Provenance of Eocene foreland basin sediments, Nepal: Constraints to the timing and diachroneity of early Himalayan orogenesis: Geology, v. 33, p. 309, doi:10.1130/G21161.1.

Nakajima, T., Fukuda, S., Sueoka, S., Niki, S., Kawakami, T., Danhara, T., and Tagami, T., 2024, Short communication: Inverse correlation between radiation damage and fission-track etching time on monazite: Geochronology, v. 6, p. 313–323, doi:10.5194/gchron-6-313-2024.

Nasdala, L., Akhmadaliev, S., Burakov, B.E., Chanmuang N, C., and Škoda, R., 2020, The absence of metamictisation in natural monazite: Scientific Reports, v. 10, p. 14676, doi:10.1038/s41598-020-71451-7.

Parrish, R.R., and Hodges, V., 1996, Isotopic constraints on the age and provenance of the Lesser and Greater Himalayan sequences, Nepalese Himalaya: Geological Society of America Bulletin, v. 108, p. 904–911, doi:10.1130/0016-7606(1996)108<0904:ICOTAA>2.3.CO;2.

Paton, C., Hellstrom, J., Paul, B., Woodhead, J., and Hergt, J., 2011, Iolite: Freeware for the visualisation and processing of mass spectrometric data: Journal of Analytical Atomic Spectrometry, v. 26, p. 2508, doi:10.1039/c1ja10172b.

Price, P.B., and Walker, R.M., 1963, Fossil tracks of charged particles in mica and the age of minerals: Journal of Geophysical Research, v. 68, p. 4847–4862, doi:10.1029/JZ068i016p04847.

Puchelt, H., and Emmermann, R., 1976, BEARING OF RARE EARTH PATTERNS OF APAT1TES FROM IGNEOUS AND METAMORPHIC ROCKS: Earth and Planetary Science Letters, p. 279–286.

Pye, A.E., Hodges, K.V., Ehlers, T.A., Van Soest, M.C., McDonald, C.S., and Bhandari, B., 2023, Constraining the exhumation history of the Greater Himalayan Sequence, Kali Gandaki, Central Nepal: Journal of the Geological Society, v. 181, p. jgs2023-100, doi:10.1144/jgs2023-100.

Pye, A.E., Hodges, K.V., Keller, C.B., Law, R.D., Van Soest, M.C., Bhandari, B., and McDonald, C.S., 2022, Prolonged Slip on the South Tibetan Detachment Constrains Tectonic Models for Synorogenic Extension in the Central Himalaya: Tectonics, v. 41, p. e2022TC007298, doi:10.1029/2022TC007298.

Pyle, J.M., 2001, Monazite-Xenotime-Garnet Equilibrium in Metapelites and a New Monazite-Garnet Thermometer: Journal of Petrology, v. 42, p. 2083–2107, doi:10.1093/petrology/42.11.2083.

Rapp, R.P., and Watson, E.B., 1986, Monazite solubility and dissolution kinetics: implications for the thorium and light rare earth chemistry of felsic magmas: Contributions to Mineralogy and Petrology, v. 94, p. 304–316, doi:10.1007/BF00371439.

Robert, X., Van Der Beek, P., Braun, J., Perry, C., Dubille, M., and Mugnier, J.-L., 2009, Assessing Quaternary reactivation of the Main Central thrust zone (central Nepal Himalaya): New thermochronologic data and numerical modeling: Geology, v. 37, p. 731–734, doi:10.1130/G25736A.1.

Robinson, D.M., DeCelles, P.G., and Copeland, P., 2006, Tectonic evolution of the Himalayan thrust belt in western Nepal: Implications for channel flow models: Geological Society of America Bulletin,.

Rubatto, D., Williams, I.S., and Buick, I.S., 2001, Zircon and monazite response to prograde metamorphism in the Reynolds Range, central Australia: Contributions to Mineralogy and Petrology, v. 140, p. 458–468, doi:10.1007/PL00007673.

Schoene, B., and Bowring, S.A., 2006, U–Pb systematics of the McClure Mountain syenite: thermochronological constraints on the age of the 40Ar/39Ar standard MMhb: Contributions to Mineralogy and Petrology, v. 151, p. 615–630, doi:10.1007/s00410-006-0077-4.

Shaulis, B., Lapen, T.J., and Toms, A., 2010, Signal linearity of an extended range pulse counting detector: Applications to accurate and precise U-Pb dating of zircon by laser ablation quadrupole ICP-MS: Geochemistry, Geophysics, Geosystems, v. 11, p. 2010GC003198, doi:10.1029/2010GC003198.

Sherpa, T.Z.L., DeCelles, P.G., Carrapa, B., Schoenbohm, L.M., and Wolpert, J., 2022, Bhumichula plateau: A remnant high-elevation low-relief surface in the Himalayan thrust belt of western Nepal: GSA Bulletin, doi:10.1130/B36481.1.

Sobel, E.R., Hilley, G.E., and Strecker, M.R., 2003, Formation of internally drained contractional basins by aridity-limited bedrock incision: Journal of Geophysical Research: Solid Earth, v. 108, p. 2002JB001883, doi:10.1029/2002JB001883.

Soucy La Roche, R., and Godin, L., 2019, Inherited Cross-Strike Faults and Oligocene-Early Miocene Segmentation of the Main Himalayan Thrust, West Nepal: Journal of Geophysical Research: Solid Earth, v. 124, p. 7429–7444, doi:10.1029/2019JB017467.

Soucy La Roche, R., Godin, L., Cottle, J.M., and Kellett, D.A., 2018, Preservation of the Early Evolution of the Himalayan Middle Crust in Foreland Klippen: Insights from the Karnali Klippe, West Nepal: Tectonics, v. 37, p. 1161–1193, doi:10.1002/2017TC004847.

Stephenson, J., Gallagher, K., and Holmes, C., 2006, A Bayesian approach to calibrating apatite fission track annealing models for laboratory and geological timescales: Geochimica et Cosmochimica Acta, v. 70, p. 5183–5200, doi:10.1016/j.gca.2006.07.027.

Stickroth, S.F., Carrapa, B., DeCelles, P.G., Gehrels, G.E., and Thomson, S.N., 2019, Tracking the Growth of the Himalayan Fold-and-Thrust Belt From Lower Miocene Foreland Basin Strata: Dumri Formation, Western Nepal: Tectonics, v. 38, p. 3765–3793, doi:10.1029/2018TC005390.

Thiede, R. C., & Ehlers, T. A., 2013, Large spatial and temporal variations in Himalayan denudation. Earth and Planetary Science Letters, 371, 278-293.

Tagami, T., 2005, Fundamentals of Fission-Track Thermochronology: Reviews in Mineralogy and Geochemistry, v. 58, p. 19–47, doi:10.2138/rmg.2005.58.2.

Vermeesch, P., 2009, RadialPlotter: A Java application for fission track, luminescence and other radial plots: Radiation Measurements, v. 44, p. 409–410, doi:10.1016/j.radmeas.2009.05.003.

Vermeesch, P., 2017, Statistics for LA-ICP-MS based fission track dating: Chemical Geology, v. 456, p. 19–27, doi:10.1016/j.chemgeo.2017.03.002.

Warren, C.J., Greenwood, L.V., Argles, T.W., Roberts, N.M.W., Parrish, R.R., and Harris, N.B.W., 2019, Garnet–monazite rare earth element relationships in sub-solidus metapelites: a case study from Bhutan: Geological Society, London, Special Publications, v. 478, p. 145–166, doi:10.1144/SP478.1.

Weise, C., Van Den Boogaart, K.G., Jonckheere, R., and Ratschbacher, L., 2009, Annealing kinetics of Kr-tracks in monazite: Implications for fission-track modelling: Chemical Geology, v. 260, p. 129–137, doi:10.1016/j.chemgeo.2008.12.014.

Whipple, K.X., 2009, The influence of climate on the tectonic evolution of mountain belts: Nature Geoscience, v. 2, p. 97–104, doi:10.1038/ngeo413.

Zhu, X.K., and O'Nions, R.K., 1999, Monazite chemical composition: some implications for monazite geochronology: Contributions to Mineralogy and Petrology, v. 137, p. 351–363, doi:10.1007/s004100050555.

Supplemental Tables

Sample	Latitude	Longitude	Elevation (m)	Unit	Lithology	Age (ma)	StdDev	Method
24KG12	28.642	83.588	2966	GHS	mylonite	0.087	0.012	MzFT
24KG12	28.642	83.588	2966	GHS	mylonite	0.336	0.028	MzFT
24KG11	28.643	83.593	2753	GHS	gneiss	0.395	0.042	MzFT
24KG10	28.647	83.594	2498	GHS	mylonite	0.246	0.018	MzFT
24KG07	28.545	83.638	1830	GHS	gneiss	0.094	0.024	MzFT
24KG07	28.545	83.638	1830	GHS	gneiss	3.03	0.44	AFT
24KG06	28.541	83.646	1540	GHS	schist	9.09	4.4	AFT

Table 1. Sample locations, elevations, lithologies, and reported ages. MzFT indicates Monazite Fission-Track age, and AFT indicates Apatite Fission-Track age.

Sample	Number of Grains	Ns	Area (cm^2)	Density of Tracks Counted	MzFT Age (Ma)
24KG07	10	3	1.11E-05	3.85E+05	0.094
24KG10	30	8.5	1.12E-05	6.40E+05	0.246
24KG11	24	10	7.86E-06	7.54E+05	0.395
24KG12	31	13.5	1.56E-05	8.71E+05	0.79 - 0.03

Table 2. Monazite Fission-Track data. Number of grains per sample analyzed, number of spontaneous track counted (Ns), median grain area in cm^2, median density of tracks per grain, and MzFT age are listed. Sample 24KG12 yielded two populations of 0.34 – 0.09 Ma.